The impacts of anomalies in atmospheric circulations on Arctic sea ice outflow and sea ice conditions in the Barents and Greenland Seas: case study in 2020

Fanyi Zhang[1,2], Ruibo Lei[2,1*], Mengxi Zhai[2], Xiaoping Pang[1], Na Li[2]

[1]Chinese Antarctic Center of Surveying and Mapping, Wuhan University, Wuhan 430079, China

[2]Key Laboratory for Polar Science of the MNR, Polar Research Institute of China, Shanghai 200136, China

Correspondence to: Ruibo Lei(leiruibo@pric.org.cn)

Abstract: Arctic sea ice outflow to the Atlantic Ocean is essential to Arctic sea ice mass budget and the marine environments in the Barents and Greenland Seas (BGS). With the extremely positive Arctic Oscillation (AO) in winter (JFM) 2020, the impacts and feedback mechanisms of anomalies in Arctic sea ice outflow on winter–spring sea ice and other marine environmental conditions in the subsequent months until early summer in the BGS were investigated. The results reveal that the total sea ice area flux (SIAF) through the Fram Strait, the Svalbard-Franz Josef Land, and the Franz Josef Land-Novaya Zemlya passageways in winter and June 2020 were higher than the 1988–2020 climatology. The relatively large total SIAF, which was dominated by that through the Fram Strait (77.6%), can be significantly related to atmospheric circulation anomalies, especially with the positive phases of winter AO and the winter–spring relatively-high air pressure gradient across the western and eastern Arctic Ocean. Such abnormal winter atmospheric circulation patterns have induced wind speeds anomalies that accelerate sea ice motion (SIM) in the Atlantic sector of Transpolar Drift, subsequently contributing to the variability of the SIAF ($R= +0.86$, $P < 0.001$). The abnormally large Arctic sea ice outflow led to increased sea ice area (SIA) and thickness in the BGS, which has been observed since March 2020, especially in May–June. The increased SIA impeded the warming of the sea surface temperature (SST), with a significant negative correlation between April SIA and synchronous SST as well as the lagging SST of 1–3 months based on the historic data from 1982–2020. Therefore, this study suggests that winter–spring Arctic sea ice outflow can be considered as a predictor of changes in sea ice and other marine environmental conditions in the BGS in the subsequent months, at least until early summer. The results promote our understanding of the physical connection between the central Arctic Ocean and the BGS.

KEYWORDS: Arctic Ocean; Sea ice; Transpolar Drift; Atmospheric circulation pattern; Barents Sea; Greenland Sea

1. Introduction

Arctic sea ice has been experiencing a dramatic loss over the past four decades, and the overall decline in sea ice extent is statistically significant in all seasons (Parkinson and DiGirolamo, 2021). In winter, due to the absence of land constraints, reductions in the Arctic sea ice extent occurred mainly in the peripheral seas, particularly in the Barents and Greenland Seas (BGS). From 1979 to 2016, sea ice changes in the Barents and Greenland Seas accounted for 27% and 23% of the total Arctic sea ice extent loss in March, respectively (Onarheim et al., 2018). Changes in Arctic sea ice may have potentially far-reaching effects not only on Arctic local climate and ecological environments but also on extreme weather or climatic events at lower latitudes (Schlichtholz, 2019). Previous studies have revealed the relations of Eurasian winter cold anomalies to sea ice reduction in the Barents Sea (e.g., Mori et al., 2014).

Through the regulations of thermodynamic and dynamic processes, large-scale atmospheric circulation patterns have significant implications on Arctic sea ice growth and decay, as well as its advection and spatial redistribution (Frey et al., 2015; Dorr et al., 2021; Dethloff et al., 2022). Dynamically, enhanced wind forcing, associated with anomalous atmospheric circulations, could enhance sea ice motility and deformation, especially for Arctic sea ice outflow through the Fram Strait (e.g., Cai et al., 2020). Associated with the conveyor belt of the Transpolar Drift (TPD), Arctic sea ice can be exported to the BGS and finally enter the North Atlantic (Kwok, 2009), which is an important mechanism for decreases in the total Arctic sea ice volume (Smedsrud et al., 2017), especially for the loss of multi-year ice (Kwok et al., 2009). Moreover, Arctic sea ice advection along the TPD is also capable of transporting ice-rafted materials or extend ice-associated biomes from the Eurasian shelf to the Arctic basin, and eventually out of the Arctic Ocean (Mørk et al., 2011; Peeken et al., 2018; Krumpen et al.,2020). The Arctic sea ice outflow, associated with equivalent fresh water outflow being comparable to that carried by the East Greenland current (Spreen et al., 2009; de Steur et al., 2014), significantly affects deep water formation in the north of the Atlantic Ocean (Dickson et al., 1988; Rahmstorf et al., 2015). In turn, the increase in the oceanic heat inflow from the north Atlantic Ocean leads to the Atlantification and promotes the retreat of sea ice in the Barents Sea (Shu et al., 2021).

As the peripheral seas of the Arctic Ocean, the BGS are not completely covered by sea ice even in winter, so the ocean dynamic processes and atmosphere-ocean interactions are relatively strong in this region compared to the central Arctic Ocean (Smedsrud et al., 2013). Sea ice outflow from the Arctic Ocean plays a crucial role in proving the preconditions of the icescape in this region. And most notably, more phytoplankton production occurs in the BGS than in other regions for the waters north of the Arctic Circle due to the supply of nutrients from the south and the availability of more photosynthetic light because of the relatively low sea ice coverage (Mayot et al., 2020; Pabi et al., 2008). Naturally, the bloom of primary productivity in this region is greatly affected by the distribution and seasonality of sea ice (Wassmann et al., 2010). Thus, further revealing the

influence and feedback mechanisms of abnormal Arctic sea ice outflow on the marine environmental conditions in the downstream of TPD over the BGS on a seasonal scale could improve the understanding of the physical connections between the central Arctic Ocean and the BGS. Such a connection is still not particularly clear, especially when some extreme atmospheric circulation events occur.

Variations in Arctic sea ice outflow to the BGS are associated with a variety of large-scale atmospheric circulation patterns and local synoptic events (Bi et al., 2016, Sumata et al., 2022), among which the atmospheric circulation patterns of the Arctic Oscillation (AO) (Kwok, 2009), the Central Arctic west-east air pressure gradient Index (CAI; Vihma et al., 2012) and the North Atlantic Oscillation (NAO; Zhang et al., 2020) can play significant roles. The AO index is the dominant pattern of surface mean air pressure anomalies, with a positive AO index indicating below normal air pressure in the Arctic and above normal over external regions (Dethloff et al., 2022). When the AO is in an extremely positive phase, the westward shift of the TPD allows thicker multi-year ice to be advected from the central Arctic Ocean towards Fram Strait (Rigor et al., 2002). In January–March 2020, the AO experienced an unprecedented positive phase, which led to the relatively rapid southward drift of the ice camp of the Multidisciplinary drifting Observatory for the Study of Arctic Climate (MOSAiC) during the winter and early spring of 2020 (Krumpen et al., 2021). The CAI, on the other hand, represents the east-west gradient of the SLP across the central Arctic Ocean, approximately perpendicular to the TPD (Vihma et al., 2012). The CAI characterizes the meridional wind forcing parallel to the TPD and so can indicate the strength of the TPD to a high degree (Lei et al., 2016). As a regional atmospheric circulation pattern, when the NAO is in positive phase, the north-south gradient of the SLP over the North Atlantic enhances, driving the sea ice southward advection through the Fram Strait (Kwok et al., 2013).

Thereby, the main objectives of this study are to clarify the effects of atmospheric circulation anomalies on Arctic sea ice outflow during winter (JFM)–spring (AMJ) 2020, and their effects on sea ice distributions and other marine conditions over the BGS in the subsequent months until early summer, in order to reveal seasonal impacts and feedback mechanisms. It should be emphasized that our study mainly focuses on the influence of atmospheric anomalies on the local sea ice mass balance in the BGS. Ocean impacts, especially the heat from the North Atlantic, is important for the seasonal changes in sea ice in the BGS. However, it is not the focus of this study. The sections of this paper are organized as follows. The datasets used to measure anomalies in atmospheric, sea ice, and oceanic conditions are briefly described in Section 2. Section 3 presents the anomalies in atmospheric circulation and Arctic sea ice outflow in the study year, as well as their influences on sea ice and oceanic conditions in the BGS. Impacts of extreme atmospheric circulation on sea ice processes before that reached the Fram Strait, other factors affecting sea ice anomalies in the BGS, and the robustness of the connections between sea ice anomalies and other marine environments identified in 2020, are discussed by comparing with the climatological data in Section 4. The

85   conclusions are given in the last section.

2. Data and methods

2.1 Study area

88   Our study focused on the downstream region of the TPD, i.e., the Barents Sea and the Greenland Sea to assess the impacts
89 of sea ice outflow from the Arctic Ocean on the sea ice and other marine conditions in this region on a seasonal scale. The
90 north-south boundaries of this region are from 72°N to the three passageways of sea ice outflow, and the east-west boundaries
91 are defined as the coastline of the surrounding islands. To quantify the sea ice outflow from the Arctic Ocean, we calculated
92 the sea ice area flux (SIAF) through the passageways, i.e., the Fram Strait, the Svalbard-Franz Josef Land (S-FJL), and the
93 Franz Josef Land-Novaya Zemlya (FJL-NZ) passageways (Figure 1), with the widths of about 448, 284, and 326 km,
94 respectively.
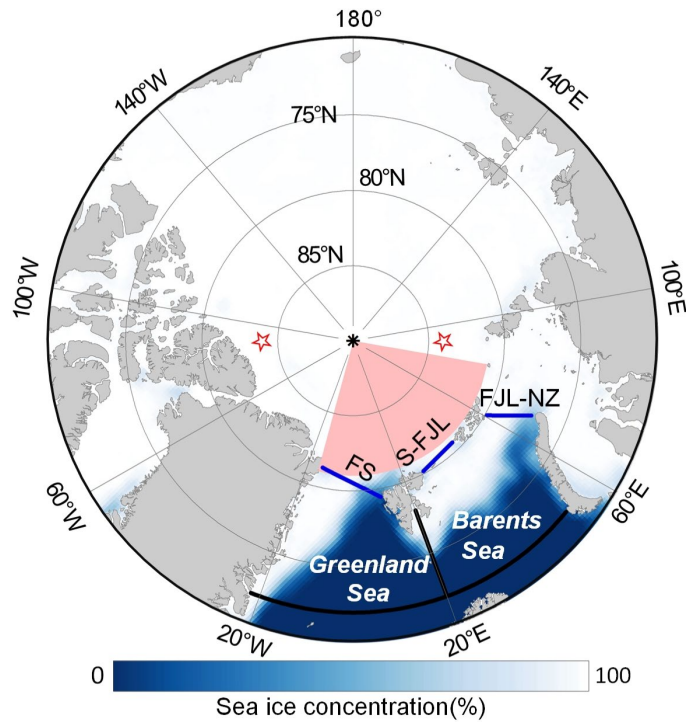
95

96 **Figure 1.** Geographical locations of the Barents and Greenland Seas. The three passageways defined for the calculations of sea ice area flux
97 are indicated by blue lines. The Barents and Greenland Seas are delimited by blue lines, black lines and the coastline. The red stars indicate
98 the locations (90° W, 84° N, and 90° E, 84°N) defined to calculate the Central Arctic west-east air pressure gradient Index (CAI). The Atlantic
99 sector of TPD from 15°W to 80°E is shaded in red. The background is the average sea ice concentration in January–March 2020.

2.2 Data

101   We used the National Snow and Ice Data Center (NSIDC) Polar Pathfinder version 4 sea ice motion (SIM) vectors and

National Oceanic and Atmospheric Administration (NOAA)/NSIDC Climate Data Record passive microwave sea ice concentration (SIC) version 4 (Tschudi et al., 2019; Meier et al., 2021) to calculate the SIAF from the Arctic Ocean to the BGS in the study year and climatological average in 1979–2020. The choice of this SIM product was motivated by its spatial completeness and temporal continuance. The SIM product is the most optimal interpolation merged result using satellite remote sensing data, buoy observations, and reanalyzed wind data (Tschudi et al., 2020). This product provides daily ice drift components georeferenced to the Equal-Area Scalable Earth Grid (EASE-Grid) with a spatial resolution of 25 km. The SIC product was a rule-based combination of SIC estimates from the National Aeronautics and Space Administration (NASA) Team (NT) algorithm (Cavalieri et al., 1984) and NASA Bootstrap (BT) algorithm (Comiso, 1986), derived from the Scanning Multichannel Microwave Radiometer (SMMR), Special Sensor Microwave Imager (SSM/I), and Special Sensor Microwave Imager/Sounder (SSMIS) radiometers. Daily SIC fields were gridded on a 25-km resolution polar stereographic grid. Both datasets are available from October 1978 to the present. However, there is a gap in the SIC dataset from 3 December 1987 through 12 January 1988. The sea ice area (SIA) was defined as the cumulative area of the waters covered by sea ice with the SIC above 15%. For the study region, we used the SIC data since 1979 to estimate the SIA anomaly from January to June in the study year of 2020. In addition, we used buoys observations data from the MOSAiC and International Arctic Buoy Program (IABP) to prove the effectiveness of the reconstructed results of the sea ice backward trajectories in the study year of 2020 and years with extreme atmospheric circulation patterns.

The sea ice thickness (SIT) data used to characterize the sea ice conditions in the BGS region was mainly derived from satellite remote-sensed observations, and supplemented by the modeling product in early summer. The remote-sensed SIT data was created from the merged CryoSat-2 and Soil Moisture and Ocean Salinity (SMOS) observations, hereinafter referred to as CryoSat-2/SMOS (Ricker et al., 2017). The CryoSat-2/SMOS dataset makes full use of the detectability of SMOS for thin sea ice (<1.0 m) and the measurement capability of CryoSat-2 for thicker sea ice, which ensures obtaining a more comprehensive product of SIT. Weekly CryoSat-2/SMOS SIT data were available on a 25-km EASE-Grid during the freezing season of October to mid-April from 2010 to the present. During the ice melt season from May–June, we used the monthly SIT modeling product obtained from the Pan-Arctic Ice Ocean Modeling and Assimilation System (PIOMAS; Zhang and Rothrock, 2003). The PIOMAS is a coupled ice-ocean model assimilation system that has been extensively validated and compared with satellite, submarine, airborne, and in situ observations, which has proved it has a good performance in sea ice thickness inversion (Zhang and Rothrock, 2003; Schweiger et al., 2011; Stroeve et al., 2014; Wang et al., 2016). The monthly PIOMAS SIT is gridded on a generalized orthogonal curvilinear coordinate system with an average resolution of 22 km. We regridded the monthly SIT data on the 25-km EASE-Grid and calculated the monthly average CryoSat-2/SMOS SIT data to maintain the spatial and

131   temporal consistency of the two SIT datasets. To assess the data consistency of these two SIT datasets, we calculated the SIT

132   anomalies from December to April using the PIOMAS SIT to compare with the CryoSat-2/SMOS SIT. We found that the

133   spatially averaged difference between PIOMAS and CryoSat-2/SMOS SIT anomalies from December to April is about 0.09–

134   0.20 m, which is about 6.0%–13.3% of the monthly magnitude. The statistical correlation between the spatially averaged SIT

135   anomalies in December–April calculated using the two datasets in 2011–2020 is 0.95 (P<0.05). Thus, we considered the

136   difference between the two datasets to be acceptable for calculating SIT anomalies, and PIOMAS can be used to supplement

137   the SIT data for the CryoSat-2/SMOS during the melt season (i.e., May–June), although their absolute values still have

138   deviations that cannot be ignored. Therefore, we used the CryoSat-2/SMOS SIT from December to April, and the PIOMAS

139   SIT from May to June in 2011–2020 to estimate the anomaly in SIT during the study year of 2020.

140   We used sea surface temperature (SST) from 2011–2020 to characterize the anomalies in oceanic condition over the BGS

141   during the study year, as SST can be used as a proxy for the physical state over a basin scale (Siswanto, 2020). The SST data

142   was obtained from NOAA Daily Optimum Interpolation SST High Resolution dataset version 2, which assimilated buoy, ship-

143   based data and satellite SST data (Huang et al., 2021). In the ice-covered regions, the proxy SST from SIC is intermixed with

144   in situ and satellite SSTs. The proxy SST is obtained by a simple linear regression with SIC (Reynolds et al., 2007), and when

145   the SIC is above 35%, the proxy SST is defined as the freezing points of seawater, which is defined using the climatological

146   sea surface salinity (Banzon et al., 2020). This dataset is available on a regular grid of 0.25°×0.25°.

147   The fifth generation reanalysis ERA5 datasets from European Centre for Medium-range Weather Forecasts (ECMWF)

148   provide sea level pressure (SLP), 2-m air temperature, 10-m surface wind, as well as atmospheric surface net heat fluxes of

149   longwave radiation, shortwave radiation, sensible heat, and latent heat (Hersbach et al., 2020). These variables, with about 30-

150   km horizontal and 1-h temporal resolutions, were used to identify anomalies in surface atmospheric conditions or forcing over

151   the study region. The ERA5 reanalysis uses an advanced 4D-var assimilation scheme, with improved performance over the

152   Arctic compared to ERA-Interim (Graham et al., 2019). The hourly SLP data from the ERA5 reanalysis were used to calculate

153   the monthly CAI, defined as the difference between SLPs at 90° W, 84° N, and 90° E, 84°N. We used the monthly AO and

154   NAO indices provided by NOAA Climate Prediction Center (CPC). The AO index was constructed by projecting a daily 1000

155   hPa height anomaly at the 20°N poles onto the AO loading pattern (Thompson and Wallace, 1998). The NAO index is defined

156   as the SLP difference between the Azores High and the Icelandic Low (Hastenrath and Greischar, 2001).

157   **2.3 Methods**

158   The SIAF was defined as the magnitude of the SIA conveyed through a defined gate during a given period. In accordance

159   with Kwok (2009), we estimated the monthly SIAF by accumulating the daily integral of the products between the gate-

160   perpendicular component of the SIM and SIC along the defined passageways. Note that there is no SIM vector when the SIC

161   is below 15% (Tschudi et al., 2019). In this case, the SIAF is ignored. Positive values correspond to the SIAF towards the BGS,

162   while negative values are the opposite. Prior to the estimation of SIAF, we interpolated the SIC into the SIM projection and

163   retrieved the gate-perpendicular SIM components. According to the trapezoidal rule, the SIAF was estimated as follows:

164    $SIAF = \sum_{i=1}^{n} u_i C_i \Delta x$ (1)

165   where n is the number of points along the passageway, u_i is the gate-perpendicular SIM component, C_i is the SIC at the

166   ith grid cell, and Δx is the width of a grid cell (25km).

167   The corresponding error of SIAF depends on the uncertainties of SIM and SIC products, the sampling number along the

168   passageways, and the calculation period. For daily SIM vectors, the error was estimated to be about 4.1 km·day^{-1} (Tschudi et

169   al., 2019). Several assessments indicated an accuracy of about 5% in the SIC (Peng et al., 2013). Assuming that these two

170   sources of error are independent, the uncertainty (σ_f) in estimating SIAF across a 1-km wide gate was estimated at about 2.92,

171   3.80, and 2.68 km^2·day^{-1} for the Fram Strait, S-FJL, and FJL-NZ, respectively. If we assume that the errors of the samples are

172   additive, unbiased, uncorrelated, and normally distributed, the uncertainty in daily SIAF is $\sigma_D = \sigma_f L / \sqrt{N_s}$ (Kwok, 2009),

173   where L is the length of the gate, and N_s is the number of independent samples across the gate. From January to June, the

174   monthly average uncertainties in SIAF through three passageways were estimated to be approximately 1.81×10^3 to 1.96×10^3

175   km^2, which were about 3.7%–13.9% of the monthly magnitude and therefore considered negligible. We described the SIAF

176   anomalies relative to the 1988–2020 climatology because differences in satellite data sources could lead to relatively low SIM

177   speeds derived from the SMMR 37-GHz data during 1979–1987 compared to that derived from daily SSM/I 85 GHz data,

178   SSMIS 91 GHz and/or AMSR-E 89 GHz observations in the later years (Kwok, 2009). To quantify the relative contributions

179   of changes in SIM and SIC to the variability of SIAF on a seasonal scale, we also calculated the correlation between the sum

180   of the monthly SIAF and the mean SIM speeds/SIC through the three passageways for winter (JFM) and spring (AMJ) in

181   1988–2020.

182   To identify the source area of sea ice and describe the relationship between the SIAF and the sea ice transport before

183   reaching the defined passageway, we also reconstructed the sea ice backward drift trajectories from the defined passageways

184   (Fram Strait, S-FJL, and FJL-NZ) over the three defined periods with the ice drifting from the north since 1 January into the

185   passageways by 30 April, 31 May, and 30 June, respectively. The adoption of three periods to restructure the ice backward

186   drift trajectories is conducive to further distinguishing the difference between the anomalies over the winter or the period of

187   winter through spring. In addition, the reconstructed backward trajectory of sea ice from the defined passageway can help to

188   identify the source area of the ice reaching the passageways, thus revealing the relationship between the sea ice outflow and

189   the sea ice conditions in the source area. The sea ice backward drift trajectories were reconstructed according to Lei et al.

190   (2019), and the zonal (X) and meridional (Y) coordinates of the backward ice trajectories were calculated as follows:

191     $X(t) = X(t+1) - U(t+1) \cdot \delta_t$ (2)

192   and $Y(t) = Y(t+1) - V(t+1) \cdot \delta_t$ (3)

193   where $U(t)$ and $V(t)$ are the ice motion components at the time t along the ice trajectories and the δ_t is the calculation

194   time step of one day. Thereby, the course of time corresponding to the sea ice backward drift trajectory is reversed from the

195   defined date to 1 January.

196   In order to reveal the contribution of surface heat budget to sea ice melting, we calculated the potential change in SIT

197   ($\triangle h$) over the time of $\triangle t$ caused by anomalies in atmospheric surface net heat fluxes over the BGS, according to Parkinson

198   and Washington (1979):

199     $-\Delta h = \frac{\triangle t}{\rho L}[\delta FL_{w\downarrow} + \delta FS_{w\downarrow} + \delta H_{\downarrow} + \delta LE_{\downarrow}]$ (4)

200   where ρ is the density of sea ice (917 kg·m^{-3}), L is the latent heat of fusion for sea ice (333.4 kJ·kg^{-1}), $\delta FL_{w\downarrow}$, $\delta FS_{w\downarrow}$,

201     $\delta H_{\downarrow}$, and $\delta LE_{\downarrow}$ represent the anomalies in atmospheric surface net fluxes of longwave radiation, shortwave radiation, sensible

202   heat, and latent heat, respectively, with the positive value denoting the downward heat flux. We note that, the Eq. 4 focuses on

203   the atmosphere-to-ice heat fluxes but ignores the effects of ocean heat flux. Thus, it can only be used to assess the impact of

204   atmospheric anomaly on the local sea ice mass balance.

205   **3. Results**

206   **3.1 Anomalies in atmospheric circulation patterns**

207   As shown in Table 1, the monthly AO was in an extremely positive phase from January to March 2020, with the values

208   ranging the top three among the years of 1979–2020. And then, the AO decreased to a smaller value in April and turned to a

209   weakly negative phase in May–June 2020 (Figure A1). Monthly CAI in January–June 2020 experienced a continuous positive

210   phase with an average CAI of 8.5 hPa, which was the largest in 1979–2020. During winter–spring 2020, there were two peaks

211   of monthly CAI occurring in March and June, ranging the first and fourth in 1979–2020, respectively.

212   In January–March 2020, accompanied by an unusual positive phase of the AO, the entire Arctic Ocean was almost

dominated by abnormally low SLP compared to the 1979–2020 climatology (the first column of Figure 2). In January 2020, a large-scale anomalous low SLP appeared near the Kara Sea, and the high-pressure center was observed in Northern North America. This SLP pattern induced a positive CAI and northerly winds from the high Arctic towards the Barents Sea, accelerating the southward advection of Arctic sea ice into the Barents Sea and causing regional negative air temperature anomalies there (the second column of Figure 2). In February 2020, the abnormally low SLP dominated near the Barents and Kara Seas, inducing strong northerly winds in the Atlantic sector of the Arctic Ocean. This SLP and wind pattern continued to promote Arctic sea ice advecting into the BGS and keeping the negative air temperature anomalies in this region. In March 2020, the low SLP anomalies moved deeper into the central Arctic Ocean and induced westerly wind anomalies in the BGS.

In April 2020, the low SLP in the Arctic, centered in the northern Beaufort Sea, caused the sea ice to continue to advect toward the Barents Sea, and there were still small-scale negative air temperature anomalies over the Barents Sea (the third and fourth columns of Figure 2). Subsequently, the SLP structure over the Arctic Ocean has changed greatly in May 2020, with high-pressure anomalies observed in the Beaufort Sea. The air temperature turned into small positive anomalies over the Barents Sea in May–June 2020. The SLP structure in May 2020 was further conducive to Arctic sea ice advection towards northeastern Greenland. This large change in SLP structure led to the prominently enhanced positive CAI, which reached the second peak in June over 1979–2020, even the AO index decreased remarkably during this period (Table 1). Therefore, the AO mainly manifests the SLP structure of the pan-Arctic, regulating the sea ice outflow from the Arctic Ocean to the BGS by changing the axis alignment of the TPD. While the CAI mainly affects the wind forcing and ice speed in the TPD region, especially for the Atlantic sector.

Table 1. Monthly AO Index and CAI in winter–spring 2020 and their ranking in 1979–2020

	January	February	March	April	May	June
AO	2.419	3.417	2.641	0.928	–0.027	–0.122
Rank	3rd	1st	2nd	7th	23th	26th
CAI/ hPa	4.219	11.317	19.671	5.387	2.219	7.942
Rank	11th	2nd	1st	19th	24th	4th

234
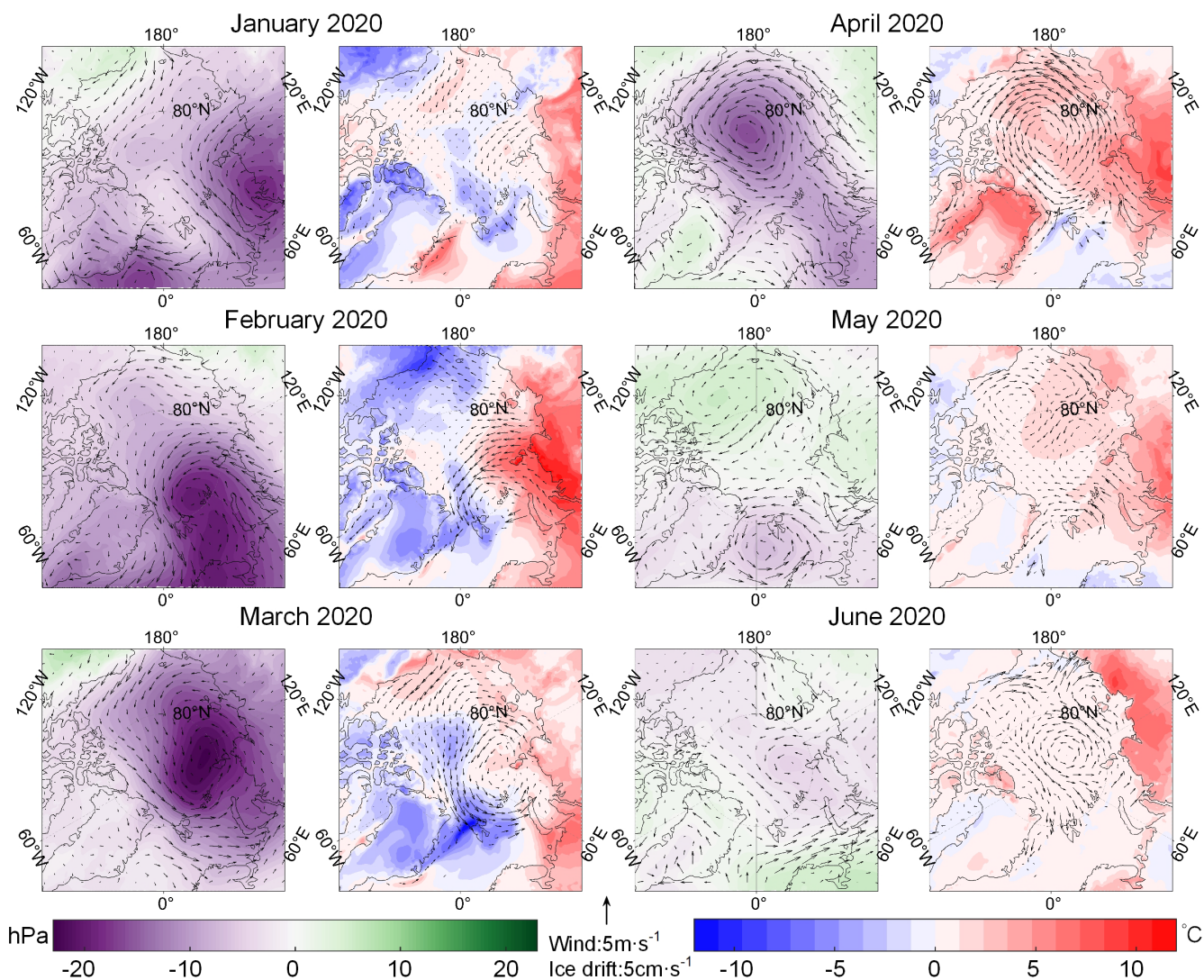
Figure 2. Monthly mean SLP (shading) and 10-m surface wind (arrows) anomalies (the first and third columns), and 2-m air temperature (shading) and sea ice drift speed (arrows) anomalies (the second and fourth columns), during January–June 2020 relative to the 1979–2020 climatology.

3.2 Anomalies in Arctic sea ice outflow and its link to atmospheric circulation patterns

The extremely positive AO in winter (JFM) 2020 induced relatively high wind speeds over the Atlantic sector of the Arctic Ocean (the first column of Figure 2), which led to the high SIM speeds along the TPD. Significant positive correlations between the monthly SIM speeds and the wind speeds in the Atlantic sector of TPD have been identified in January–February, April and June, as shown in Table A1. The 1988–2020 data revealed that the SIM speeds perpendicular to the passageways is significantly correlated with the accumulated SIAF through three passageways in both winter and spring (R=+0.86, +0.85, respectively; P<0.001), while the corresponding correlation between SIC and the SIAF is only significant in winter (R=+0.42, P<0.05). In January–June 2020, SIC anomalies contributed 3.9 % to SIAF anomalies and SIM speed anomalies contributed 71.7%. The anomalies of Arctic sea ice outflow through our defined passageways were mainly dominated by SIM anomalies

247 in winter–spring 2020. Compared to the 1988–2020 climatology, the accumulated SIAF across three passageways was all at

248 the above-average level in January–March and June, with the largest positive anomalies occurring in March 2020.

249   In winter 2020, the cumulative SIAF through the Fram Strait was 1.19×10^5 km^2, which was larger than the 1988–2020

250 average by about 20%, and was the second largest in 2010–2020. Especially in March 2020, the monthly SIAF through the

251 Fram Strait (5.77×10^4 km^2) reached the second largest in 1988–2020. The winter cumulative SIAF through S-FJL in 2020

252 (1.51×10^4 km^2) also was the second largest in 2010–2020. However, the winter cumulative SIAF through the FJL-NZ in 2020

253 (2.76×10^4 km^2) was only about 81.0% of the 1988–2020 average. That is, the extremely positive AO in winter 2020 only

254 significantly facilitated more sea ice outflow through the Fram Strait and S-FJL, while sea ice outflow through the FJL-NZ

255 did not respond significantly to the extremely positive AO. Under the influence of positive CAI in spring (AMJ) 2020, the

256 cumulative SIAF through the Fram Strait was still at an above-average level. While the spring cumulative SIAF through the

257 S-FJL and FJL-NZ in 2020 was only 67.5% and 14.1% of the 1988–2020 average, respectively. Such low SIAF through the

258 FJL-NZ passageway may be related to the enhanced inflow from the Barents Sea into the Arctic Ocean through this passageway

259 (Polyakov et al., 2023). This implies that the SIAF through these two passageways, especially for the FJL-NZ passageway in

260 the east, was not facilitated by a positive CAI in spring 2020.

261   Overall, the total SIAF anomalies in January–June 2020 were most pronounced in the Fram Strait, followed by those

262 observed in the S-FJL passageway, with positive anomalies of 2.35×10^4 and 1.40×10^4 km^2 (Figure 3), respectively. However,

263 negative anomalies were observed in the FJL-NZ passageway. This indicates that only the SIAF through the Fram Strait and

264 S-FJL responds to both the extremely positive phase of winter AO and the continuous positive phase of the winter–spring CAI.

265 Furthermore, the values of the total SIAF anomalies in January–June 2020 through these three passageways were not prominent

266 in 1988–2020 (last row of each panel in Figure 3). This implies such discontinuous extreme AO and CAI only had a moderate

267 impact on the Arctic sea ice outflow through these three passageways, especially the FJL-NZ in the east.

268   We further quantified the relationship between SIAF and two atmospheric circulation indices (AO and CAI) from 1988

269 to 2020 to test the robustness of the influencing mechanism identified in 2020. Here, we chose the Fram Strait as the

270 investigated passageway. Because in winter–spring 2020, the Fram Strait contributed the most (77.6%) to the total SIAF

271 through the three passageways. We calculated the correlation coefficient (R) between the detrended monthly SIAF and the

272 detrended AO and CAI from January to June for the period 1988–2020 (Table 2). During January–June, there was a significant

273 positive correlation between SIAF and the AO identified in February, but not in other months. This is consistent with a weak

274 linkage between the AO and SIAF through the Fram Strait in 1979–2014 (Polyakov et al., 2023). There was also a significant

275 positive correlation between monthly SIAF and CAI in January, March and April (R=0.61, 0.40, and 0.54, respectively; $P <$

276 0.05), which suggests that the relatively high CAI could induce a southward advection of Arctic sea ice to the BGS, especially

277 during the period (March–April) with a relatively high ice motion speed in the regions north of the BGS compared to other

278 months (e.g., Lei et al., 2016).
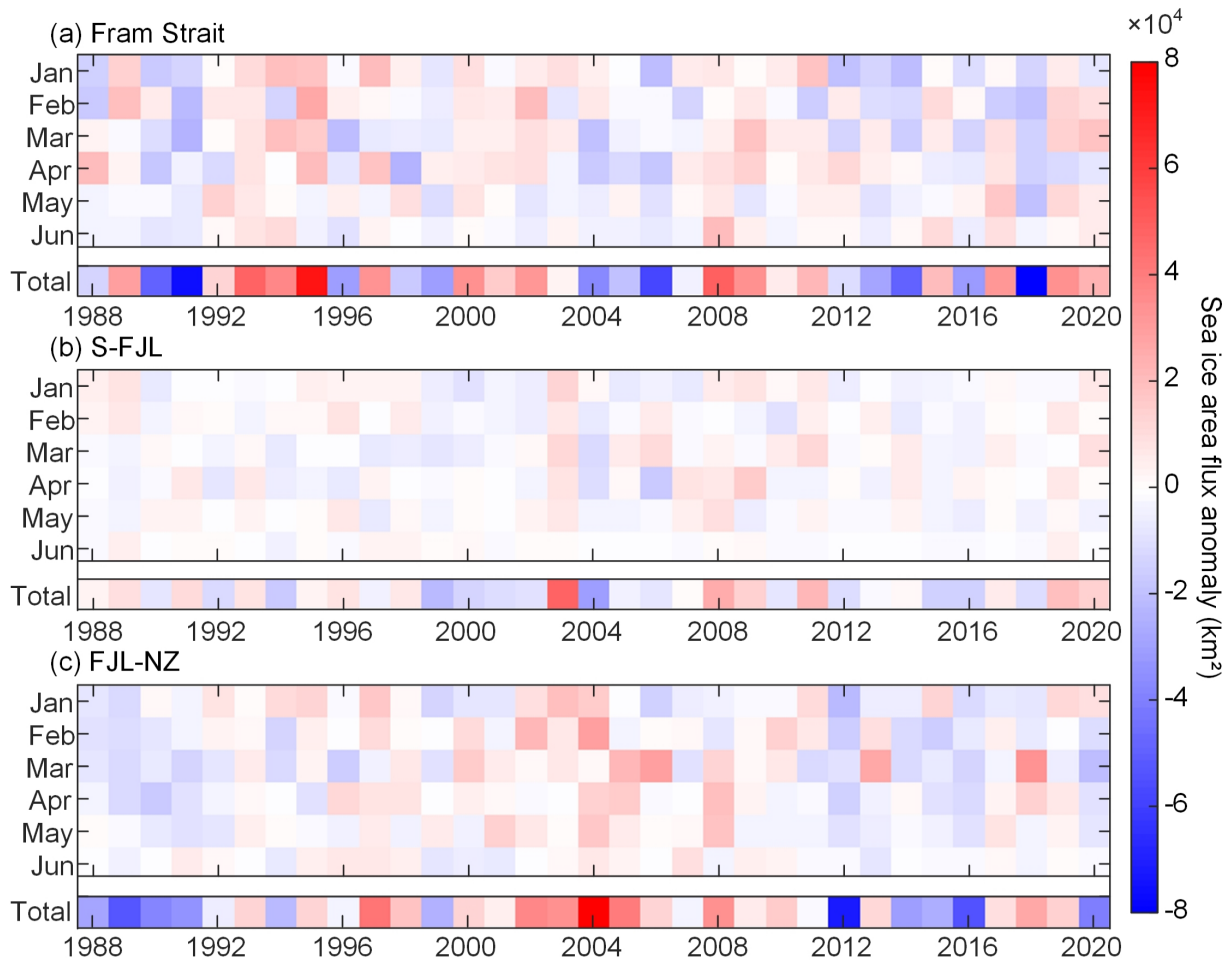
Figure 3. Monthly anomalies of sea ice area flux (SIAF) through the Fram Strait, S-FJL, and FJL-NZ from 1988 to 2020. The last row of
each panel represents the anomalies of cumulative SIAF from January to June.

Table 2. Correlation coefficient (R) between monthly sea ice area flux (SIAF) through the Fram Strait and atmospheric circulation indices
in 1988–2020

Month	January	February	March	April	May	June
AO	n.s.	0.437*	n.s.	n.s.	n.s.	n.s.
CAI	**0.610**	n.s.	0.403	*0.538*	n.s.	n.s.

Note: Significance levels are $P < 0.001$ (bold), $P < 0.01$ (italic) and $P < 0.05$ (plain); n.s. denotes insignificant at the 0.05 level.

3.3 Anomalies in sea ice backward trajectories from the passageways

The sea ice backward trajectories can be traced back to the source region of sea ice that advected to the passageways. The

broader distribution of the sea ice original area implies that more ice would enter the passageways, leading to an increased sea

288 ice outflow. The reconstructed sea ice backward trajectory in January–June 2020 was similar to that of the MOSAiC ice station

289 (Nicolaus et al., 2021) in the same period, with almost parallel orientation and very close drift distance between them (Figure

290 4c). The slight dislocation was mainly attributed to the inconsistent termination location between the reconstructed backward

291 trajectory and the MOSAiC trajectory on 30 June 2020. Using the endpoints of the two buoys obtained from MOSAiC as the

292 start points of the reconstructed backward trajectories, the Euclidean distance between the termination locations of the

293 reconstructed backward trajectory and the starting locations of the buoy trajectories is averaged out at 63 km, and their

294 trajectories almost overlapped, with the cosine similarity between them reaching 0.85. We also compared the consistency

295 between the reconstructed backward trajectories and the buoys trajectories, with the data obtained from International Arctic

296 Buoy Program, when the extreme positive or negative (± 1 *standard deviation*) phase of AO and CAI occurred (hereinafter

297 referred as AO+, AO–, CAI+ and CAI–). As shown in table A2, in the AO+ and CAI+ cases, the average Euclidean distances

298 between the reconstructed backward trajectories and buoy trajectories were smaller than in the AO– and CAI– cases. This

299 indicates that the sea ice drift distances obtained from the reconstructed backward trajectories are closer to the buoys

300 observations in the AO+ and CAI+ cases than in the AO– and CAI– cases, because the tortuous sea ice trajectories were

301 relatively large under the AO– and CAI– than under the AO+ and CAI+. However, the cosine similarities were above 0.9 in

302 all AO and CAI cases. This suggests that the orientation of the reconstructed backward trajectories is reliable regardless of the

303 phases of AO and CAI. It increases our confidence in using this method to reconstruct the ice backward trajectories to identify

304 the source region of sea ice.

305 Compared to the sea ice backward trajectories reconstructed using the average SIM vector of 1988–2020 (Figure 4d–4f),

306 the sea ice backward trajectories from the Fram Strait in 2020 tended westward (Figure 4a–4c). This implies that the orientation

307 of TPD was more favorable for exporting thicker ice from the western Arctic Ocean and northern Greenland to the Fram strait

308 during winter–spring 2020. For the Fram Strait, the terminations of the sea ice backward trajectories in 2020 were concentrated

309 at 87°–90°N, which indicates that most of the sea ice advected into this passageway was from the region close to the North

310 Pole. In all three investigation periods, the net distances from the start points at the defined passageways to the terminations

311 of the reconstructed ice backward trajectories in 2020 were the second longest in 1988–2020. In S-FJL, sea ice was mainly

312 advected from the confluence of the Kara Sea and the central Arctic Ocean (Figure 4), and its backward trajectories were

313 curved than that from the Fram Strait. Furthermore, no reasonable backward trajectories of sea ice could be acquired for the

314 S-FJL passageway according to the starting points of 31 May and 30 June. It was because the relatively low SIC in this region

315 by late spring had restricted the acquisition of valid SIM data. The sea ice advected through the FJL-NZ passageway was

316 mainly from the Kara Sea. Thus, the identifications of the source area of sea ice that reaching the passageways can explain

317   why the changes in SIAF through the S-FJL and FJL-NZ passageways are not so sensitive to changes in the CAI pattern than

318   that through the Fram Strait.

319   Overall, compared to the 1988–2020 averages, the sea ice backward trajectories through the Fram Strait in winter–spring

320   2020 were characterized as longer and farther west. Especially, the net distances between the terminal points on 1 January and

321   the starting points from Fram Strait since 30 April, 31 May, and 30 June of each year in 1988–2020 were significantly positively

322   correlated with the corresponding SIAF (R = +0.80, +0.72, +0.75, respectively; P < 0.001). Thus, the enhanced sea ice motion

323   along the TPD during January–June 2020 promoted more Arctic sea ice export toward the BGS, which in turn accelerated the

324   reduction of sea ice over the pan Arctic Ocean.
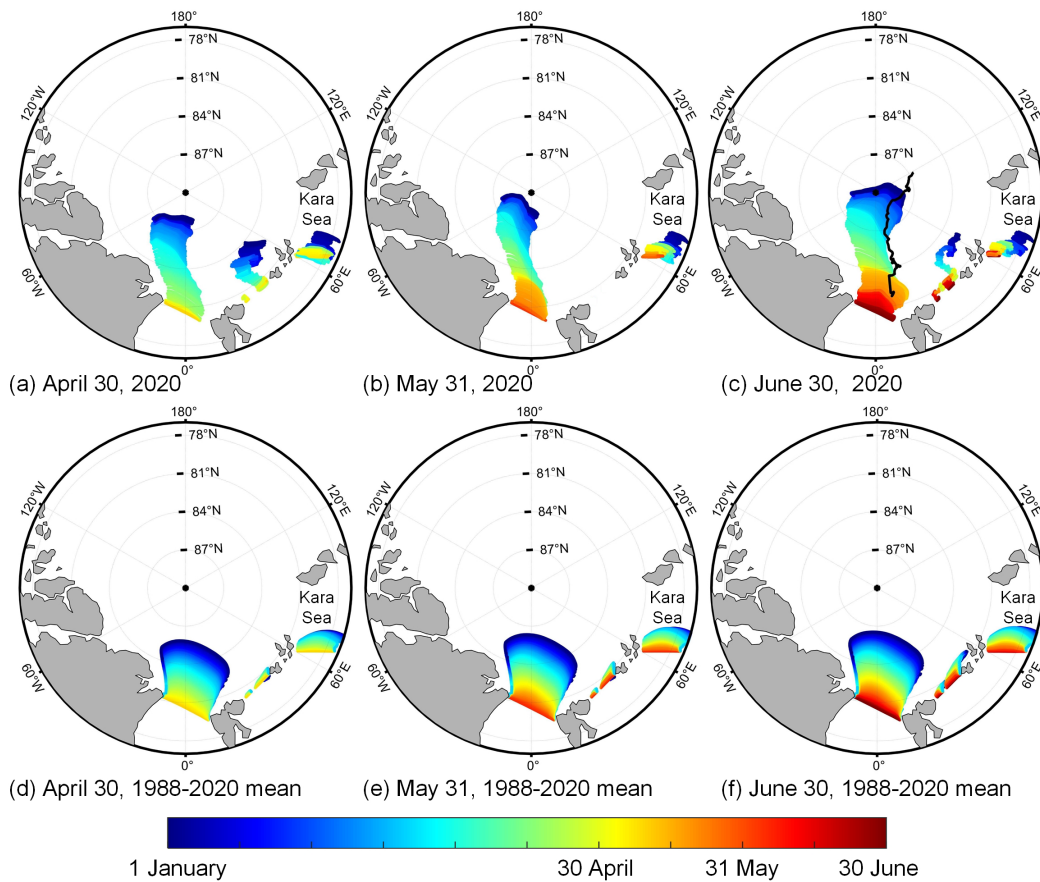
325

326   **Figure 4.** Backward trajectories of sea ice advected to the Fram Strait, S-FJL, and FJL-NZ passageways. The first row shows the backward

327   trajectories of sea ice arriving at the passageways by 30 April, 31 May and 30 June 2020, respectively. The second row is the same as the

328   first row but estimated using the average sea ice motion vector from 1988 to 2020. All termination date of the reconstructed backward

329   trajectories were set to January 1. The black line in panel (c) represents the MOSAiC trajectories from January 1 to June 30, 2020.

330   **3.4 Anomalies in sea ice and sea surface temperature in the Barents and Greenland Seas**

331   SIA in the BGS generally reaches its annual maximum in April each year, and then begins to decline as the air and ocean

332   temperature rises. In April–June 2020, the SIA in the BGS reached the first, second and the fourth largest in 2010–2020. It was

333 much higher compared to the value obtained from the linear decreasing trend from 1979 to 2020, indicating that the SIA at the

334 study year was relatively higher than the expectation. In the Barents Sea, the monthly SIA values for January–April 2020 all

335 ranged the top three in 2010–2020 (Figure 5a). The SIA in the Greenland Sea was similar to that in the Barents Sea, with

336 monthly SIA values in April–June 2020 ranking the first or second largest in 2010–2020. Such a large SIA in the BGS during

337 spring 2020 was linked to a more massive sea ice export from the central Arctic Ocean, because we found a significant

338 correlation ($R = +0.37$, $P < 0.05$) between the total SIAF anomalies through the three defined passageways and the SIA in the

339 BGS based on the 1988–2020 data.
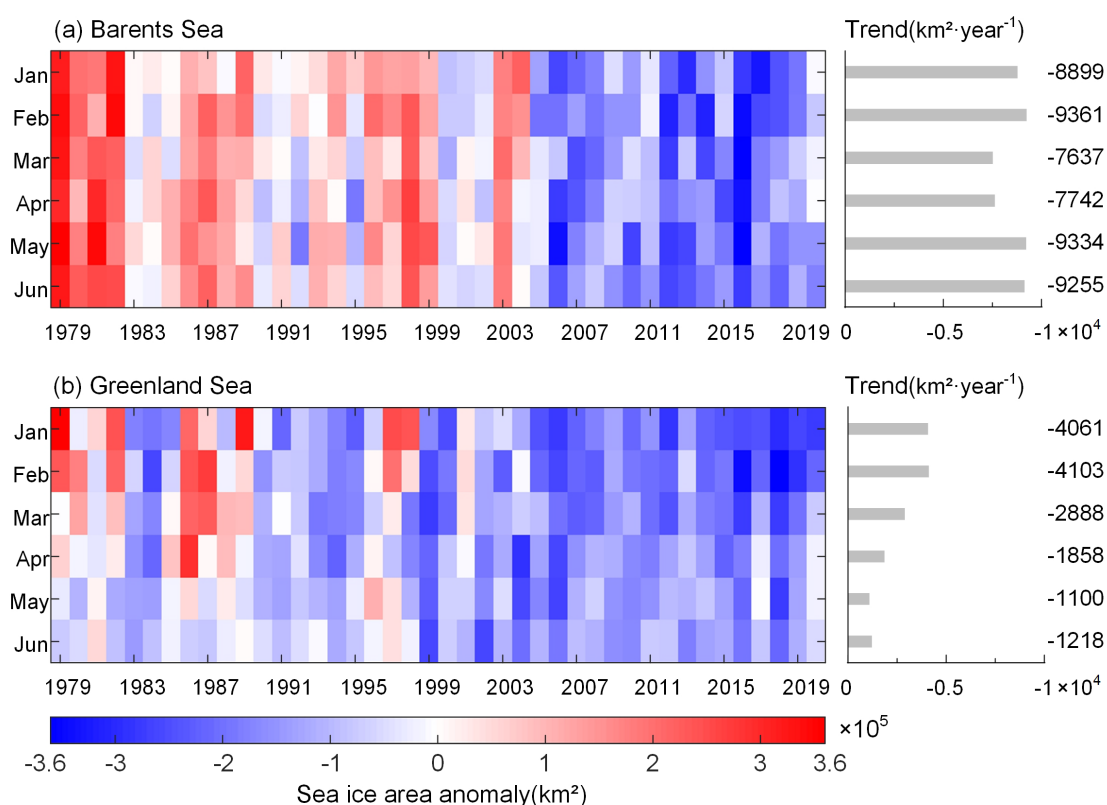
340

341 **Figure 5.** Monthly sea ice area (SIA) anomalies in the Barents and Greenland Seas from 1979 to 2020. Also shown on the right are the

342 corresponding long-term linear trends, which are all statistically significant at the 0.05 level.

343   As shown in Figure 6, negative SIT anomalies, i.e., ice thinner than the average, were observed mainly in the Greenland

344 Sea during December 2019. The SIT anomalies were relatively small in the Barents Sea. Since January 2020, more pronounced

345 positive SIT anomalies, i.e., ice thicker than the average, were observed in the Barents Sea and persisted to June. In the

346 Greenland Sea, the positive SIT anomalies gradually increased, particularly in the eastern side since March 2020 and were

347 especially widespread in May–June, while the negative SIT anomalies were mainly observed in the western side. This east-

348 west pattern of SIT anomalies could be attributed to the increased outflow of thicker sea ice from the central Arctic through

349 the Fram Strait.

350   Furthermore, widespread negative anomalies of SST (–1°C to –3 °C, Figure 7) were observed in the BGS in April–June

351   2020, with monthly SSTs being the lowest in 2011–2020.In addition, the negative SST anomalies over the Greenland Sea

352   persisted until July 2020. The detrended correlations between the monthly SIA and contemporaneous SST in the BGS from

353   April to June over 1982–2020 (Table A3) were significantly negative. Thus, the abnormally large Arctic sea ice outflow in

354   winter–spring 2020 led to an increased SIA and the associated relatively high albedo in the BGS, thereby preventing the

355   absorption of solar radiation by the ocean and suppressing the rise in SST. In turn, relatively colder seawater was not conducive

356   to sea ice melting there. The corresponding correlation coefficients in the Greenland Sea were weaker compared to those in

357   the Barents Sea, which may be due to the relatively complex influence factors on the SST variations in the Greenland Sea.

358   That is to say, the northwestern Greenland Sea is suppressed from cooling effects due to sea ice and surface current outflow

359   from the north, while the southeastern part is subject to warming effects from warm Atlantic waters (Wang et al., 2019).

360   Regionally, we found that the negative correlation coefficients between SIA and SST are more significant in the southern BGS

361   (72°–76°N) than in the northern part (76°–80°N). This is likely because the SST is more closely correlated with the SIC in

362   areas with less sea ice (Wang et al., 2019). In addition, we examined the statistical relationship between the detrended April

363   SIA and the detrended monthly SST with a lag of 1–3 months in the BGS (Table A4). In the Barents Sea, the April SIA still

364   had a significant negative effect on the increase in SST until July, i.e., with a lag of 3 months, whereas in the Greenland Sea,

365   the significant influence of April SIA on the SST only lasted until June. This difference suggests that the sea ice anomalies in

366   the Barents Sea have a longer memory for the impact on the SST than those in the Greenland Sea.
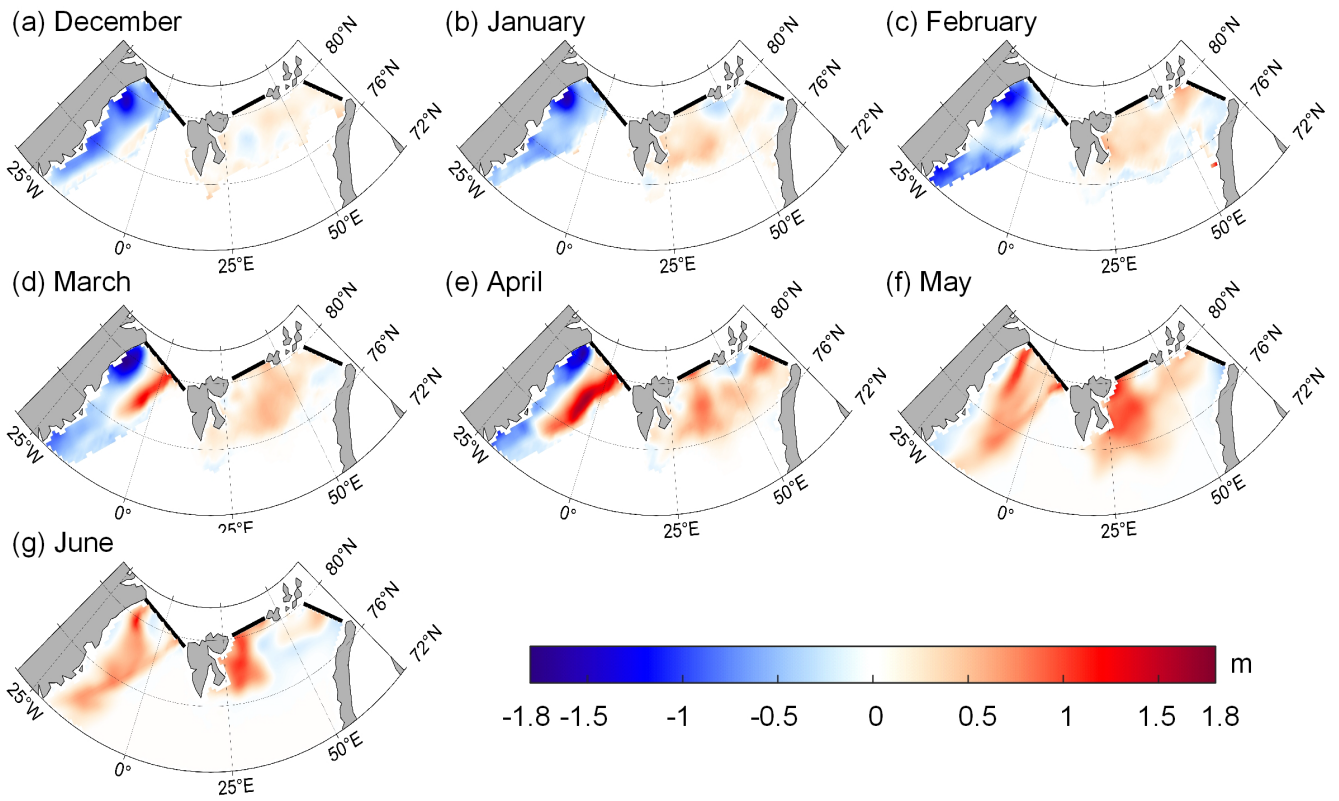
Figure 6. Sea ice thickness (SIT) anomalies in the Barents and Greenland Seas from December 2019 to June 2020 compared to the 2011–2020 average obtained from the CryoSat-2/SMOS product (December–April) and PIOMAS modeled data (May–June).
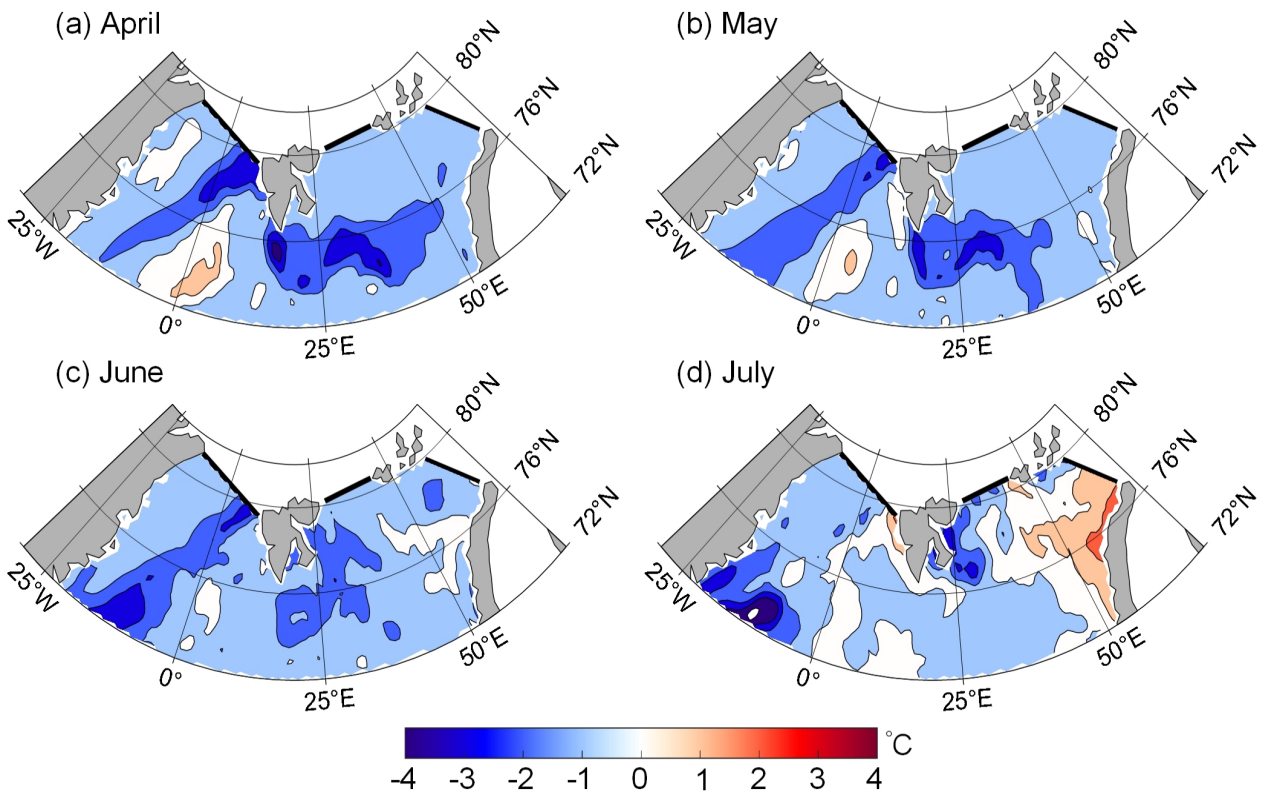
Figure 7. Monthly sea surface temperature (SST) anomalies in the Barents and Greenland Seas from April to July 2020 compared to the 2011–2020 average.

4. Discussion

4.1 Impact of extreme atmospheric circulation patterns on sea ice processes before that reached the Fram Strait

To explore the changes in sea ice backward trajectories in response to extreme atmospheric circulation patterns, we examined the years in which AO+, AO–, CAI+, CAI– occurred in winter, based on which we obtained the mean SIM field and reconstructed the January–June sea ice backward drift trajectories arriving in the Fram Strait in June of the corresponding years (Figure A2). In the AO+ case, the end of sea ice backward trajectories (blue trajectory in Figure A2a) extended westwards, which indicated that the TPD originated further west. This suggests that the winter AO+ is more conducive to sea ice outflow from the central Arctic Ocean to the BGS (e.g., Rigor et al., 2002). Thus, we believe the relationship between the positive phase anomalies of AO and the westward alignment of TPD identified in 2020, as shown in Figure 4, is robust. Whereas in the AO– case, the sea ice backward trajectories were closer to the prime meridian and relatively eastward compared to the AO+ case. Under the influence of AO–, the expanding Beaufort Gyre can weaken the strength of the TPD and reduces Arctic sea ice export (e.g., Zhang et al., 2022). Associated with either the CAI+ or CAI–, the sea ice backward trajectories were similar to those under the corresponding phase of the AO. However, in the two investigated periods of January–May and January–June, there is a higher positive (negative) correlation between the latitude (longitude) of sea ice backward trajectories endpoints and the CAI compared to the AO (Table A5). This relationship was due to the fact that the CAI+ might directly enhance the TPD by strengthening the straight-forward wind forcing, hence favoring sea ice outflow from the central Arctic Ocean into the Fram Strait. However, the insignificant correlation between them was obtained in the investigated period of January–April. It is likely related to the fact that the sea ice backward trajectories reconstructed in this period were relatively short and the variations in the backward trajectory endpoints between the years were relatively small.

The January–June average sea ice backward trajectories in AO+, AO–, CAI+ and CAI– cases were then used to further check whether extreme atmospheric circulation patterns have influences on the atmospheric forcing of sea ice thermodynamic process. We obtained the Freezing Degree Days (FDD), which was the temporal integral of air temperature below the freezing point over the freezing season. The results showed that, only the FDD in the AO+ case (2616 K·day) was lower than the 1988–2020 mean (2695 K·day). This implies that the endpoint of the backward trajectory corresponding to the AO+ would be further south and east (Figure A2), the near-surface air temperature over there would be significantly higher than that in the northwest, which was unfavorable for sea ice growth. We also compared the lengths of time that the sea ice backward trajectory within the region south of 82°N before the floe reached the Fram strait, as sea ice there was affected by strong heat supply from the ocean (Sumata et al., 2022). In the AO+ (CAI–) case, the residence time in the region south of 82°N before ice reaching the Fram Strait was 54 (57) days, which is longer than in the AO– (CAI+) case (43 (38) days). This suggests that sea ice in the

402   AO+ or CAI– cases was exposed to strong heat from the ocean for a longer period, and therefore facilitating larger sea ice melt

403   than in the AO– or CAI+ cases.

4.2 Other factors affecting sea ice anomalies in the Barents and Greenland Seas

405   The impact of Arctic sea ice outflow on the SIA in the BGS would be weakened by both local atmospheric and oceanic

406   forcing (Fery et al., 2015; Lind et al., 2018). Here, we focus on the effect of atmospheric anomalies on sea ice conditions. The

407   persistence of negative air temperature anomalies in the BGS from February to April 2020 (the second and fourth columns of

408   Figure 2), roughly 2 to 6 ℃ lower than the 1979–2020 climatology, would restrict the sea ice melting there. Especially in

409   March 2020, negative air temperature anomalies covered almost the entire BGS, and the region with the –6 ℃ anomalies

410   occurred in the coincident region with positive monthly SIT anomalies (Figures 2 and 6). Moreover, compared to the 1979–

411   2020 climatology, the monthly atmospheric surface heat fluxes showed positive (upward) anomalies over the climatological

412   ice-covered BGS (regions with the SIC above 85% for 1979–2020 climatology) in January–March 2020 (Figure 8), which

413   were mainly dominated by turbulent heat flux (35.7–38.6W·m^{-2}), accounting for 84.2%–98.9% of the atmospheric surface heat

414   flux anomalies. Especially, in February and March 2020, the upward anomalies in sensible heat flux were 1.7–2.4 times of

415   latent heat flux. This was likely due to the relatively large air-sea temperature difference and relatively high wind speeds in the

416   BGS during this period, which would result in an unstable atmospheric boundary layer and the increased atmospheric heat flux

417   from the ocean to the air (Minnett and Key, 2007). In addition to turbulent heat flux, the net longwave radiation revealed

418   relatively small upward anomalies (0.4–8.9 W·m^{-2}) persisting from January to April 2020, which was also favorable for

419   preventing ocean warming and ice melting. From April to June 2020, the direction of monthly anomalies in atmospheric surface

420   heat fluxes shifted from upward to downward, but the values are smaller relative to the values in January–March. It is worth

421   noting that, upward anomalies in net shortwave radiation were observed in June 2020 over the study region, which coincided

422   with the relatively large SIA and the associated relatively high regional albedo. Over the climatological ice-covered BGS,

423   anomalies in the cumulative monthly atmospheric surface heat flux from January to April 2020 were associated with a reduced

424   decrease of 0.12–0.51 m in SIT, estimated using Equation 4. It was conducive to the survival of sea ice during spring and early

425   summer 2020.

426   The NAO did not exhibit an extreme positive phase in 2020. However, we still investigated the relationship between the

427   NAO index and the sea ice condition in the BGS, considering the regional influence of the NAO on the BGS. In 2020, the

428   NAO index remained positive from January to March, similar to the positive AO index. It favored Arctic sea ice outflow to

429   the BGS to some extent, as a significant positive correlation (R=0.36, P<0.05) between the NAO index and the SIA in the

430   southern BGS was identified in January. The positive phases of NAO in January–March also induced a stronger northerly wind

431   over the North Atlantic, carrying cold air southward and thus decreasing the air temperature in the BGS (e.g., Hurrell, 2015).

432   As shown in the second column of Figure 2, which was not conducive to sea ice melting. Thus, the NAO mainly regulates the

433   wind forcing of BGS, rather than the atmospheric forcing before sea ice reaches our defined passageways, as the AO and CAI

434   do.
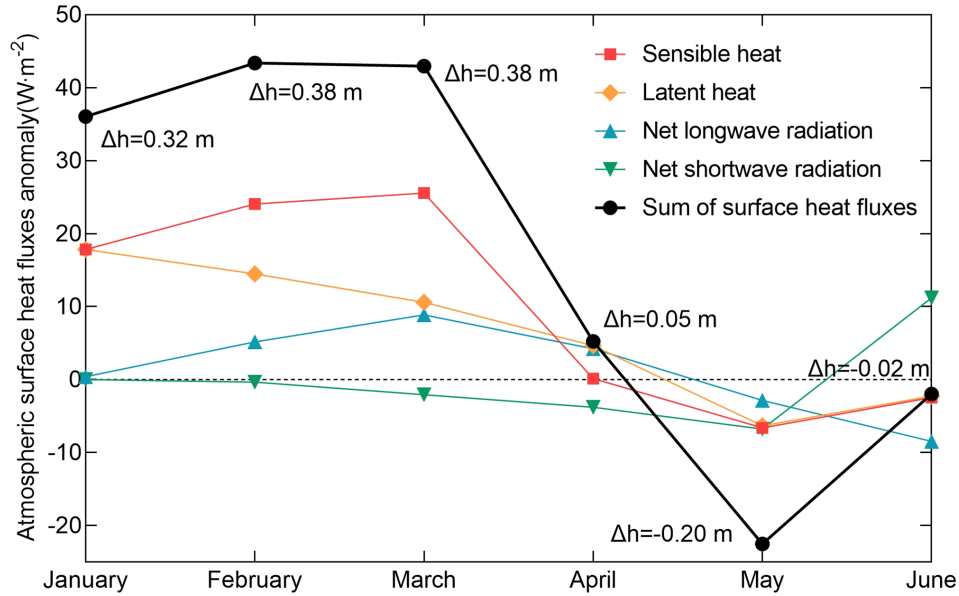
435

436   **Figure 8.** Monthly anomalies in atmospheric surface heat fluxes of sensible heat, latent heat, net longwave radiation, and net shortwave

437   radiation averaged over the climatological ice-covered region of BGS from January to June 2020 compared to the 1979–2020 average, with

438   positive values denoting the upward fluxes. Δh refers to the changes in SIT estimated from Equation 4 based on the sum of atmospheric

439   surface heat fluxes anomaly of the corresponding month.

440   **4.3 Are the anomalies and their connections identified in winter–spring 2020 typical in climatology?**

441   In the past decade, positive anomalies in the winter–spring SIAF through our defined passageways relative to the 1988–

442   2020 climatology were also identified in 2011, 2017, and 2019, close to the value in 2020 (Figure 3). Therefore, we also

443   quantified the anomalies of sea ice and ocean conditions in the BGS for these years to assess the robustness of the seasonal

444   feedback mechanisms identified in winter–spring 2020. During these three years, the sea ice backward trajectories

445   reconstructed starting since 30 April, 31 May, and 30 June were also characterized as longer and farther west compared to

446   1988–2020 climatology. This suggests that the ice speeds along the TPD were relatively large and could partially contribute to

447   the positive SIAF anomalies in these years. In the BGS, although small negative SIA anomalies were observed in March–June

448   2011, 2017, and 2019 compared to the 1979–2020 climatology, their values were still much higher than those estimated from

449   the long-term linear decreasing trends since 1979 by 0.16×10^4–2.95×10^4, 0.33×10^5–1.41×10^5 and 0.71×10^5–1.09×10^5 km^2,

450   respectively. During these three years, similar upward anomalies in accumulated net atmospheric surface heat fluxes were also

451   identified in January–March, suggesting the potential coupling mechanism between sea ice coverage and surface heat budget

452   in the BGS. However, compared to the 1979–2020 climatology, there were positive air temperature anomalies in January–

453   March 2011, 2017, and 2019, in contrast to the negative air temperature anomalies in 2020. This may subsequently contribute

454   to the relatively small negative SIA anomalies in these years than in 2020. The SIT anomalies were calculated only for 2017

455   and 2019 since satellite SIT data were not available prior to 2011, and we found that the BGS also showed small positive

456   anomalies from March to June for both years compared to the average since 2011. Furthermore, the sea ice anomalies in these

457   years also had impacts on the oceanic conditions of the BGS in subsequent April–June. The monthly SSTs in May–June of

458   2011, 2017, and 2019 all ranked the 2nd–4th lowest in 2010–2020.

459   For comparison purposes, the extremely negative SIAF anomalies through the defined passageways in winter–spring

460   should also be taken into consideration, we thus chose the year of 2018 as the case of low Arctic sea ice outflow (Figure 3). In

461   2018, the sea ice backward trajectories were all shorter than 1988–2020 climatology over all the periods of January–April,

462   January–May, and January–June. This suggested that the southward SIM speeds along the Fram Strait was relatively low from

463   January to June in 2018 (Sumata et al., 2022). In the BGS, the SIA in May–June 2018 was lower by 4.44×10^4 and 3.63×10^4

464   km^2 compared to the SIA estimated from the long-term linear decreasing trends since 1979. In January–June 2018, there were

465   widely negative SIT anomalies in the BGS compared to the 2011–2018 climatological mean, which is consistent with the

466   abnormal SIT reduction in the Fram Strait region confirmed by Sumata et al., (2022). The oceanic condition in the BGS was

467   also affected. In May, the mean SST in 2018 was higher than that in the high outflow cases (2011, 2017 and 2019) by 20%–

468   40%, consistent with the negative correlation between SIA and SST (Table A3).

469   We also assessed the impact of positive AO in summer (JAS) on the BGS, since sea ice motion generally responds more

470   strongly to the atmosphere in summer. Using the year of 2016 in which AO+ occurred in summer, we found that the SIAF

471   through Fram Strait in this summer was much larger than the 1988–2020 climatology, ranking the third and fourth in 1988–

472   2020. This suggests that AO+ also contributes to the enhanced Arctic sea ice outflow to some extent in summer. However, due

473   to local processes, the BGS SIA in this summer was even smaller than that estimated from the linear regression of 1979–2020.

474   Note that, we also expect that the influences of abnormally high Arctic sea ice outflow on the sea ice and other marine

475   conditions in the BGS will gradually weaken if the Arctic sea ice continues to thin and the northward Atlantic Ocean heat flow

476   continues to increase, because the thinner ice under the increased oceanic heat would not be conducive to the survival of sea

477   ice in the BGS.

5. Conclusions

In this study, we investigated the impacts of atmospheric circulation anomalies on Arctic sea ice outflow in the winter and spring of 2020, assessed anomalies in sea ice and oceanic conditions in the TPD downstream region of the BGS and the linkages between them, and then discussed the factors contributing to the sea ice anomalies in the BGS.

Compared to the 1979–2020 climatology, the AO experienced an unusually large positive phase in January–March 2020. In the context of this, the SLP structure, associated with the positive CAI induced strong northerly winds along the Atlantic section of TPD, leading to enhanced SIM speeds, which then facilitated Arctic sea ice outflow to the BGS. The variabilities of seasonal accumulated SIAF in 1988–2020 through these passageways were mainly dominated by the change in SIM speed (R = +0.86 for January–June; $P < 0.001$), which was more significant than that related to the changes in SIC (R = +0.42 for January–March; $P < 0.05$). In the following three months, the AO decayed to be negative, while the CAI remained positive, which ensured a continuous enhanced Arctic sea ice outflow to the BGS. Therefore, in January–March and June 2020, the total SIAF through three passageways north of the BGS was relatively large compared to the 1988–2020 climatology, mainly through the Fram Strait. The SIAF through the Fram Strait was significantly positively correlated with AO in February, and with CAI in March and April ($P < 0.05$) in 1988–2020. The total SIAF anomalies in January–June 2020 through the Fram Strait and S-FJL passageways were relatively pronounced, but their values ranged sixth to twelfth over the 1988–2020 period, which doesn't seem to be prominent. This implies that the SIAF is also regulated by other factors, such as the persistence of atmospheric circulation patterns and the coordination mechanism between AO and CAI.

The abnormal atmospheric circulation patterns had an impact on both the dynamics and thermodynamic processes of sea ice before it reached the passageways. Dynamically, under the positive phases of AO and CAI in winter and/or spring 2020, the sea ice backward trajectories reaching Fram Strait were relatively longer and sloped westward compared to the 1988–2020 climatology, which reflects the larger ice speed along the TPD and the orientation of the TPD favoring Arctic sea ice outflow to the BGS. This regime also manifests that AO affects Arctic sea ice outflow by modifying the axis alignment of TPD, while the CAI directly affects the wind forcing in the TPD region. Thermodynamically, in the AO+ case, the FDD obtained along the backward trajectory were lower than those obtained without the influence of abnormal AO and CAI, which is unfavorable for sea ice growth. In the AO+ and CAI– cases, ice floes remained in the region south of 82°N before reaching Fram Strait for a longer period of time, with the sea ice suffering from an enhanced oceanic heat in this relatively south region (Sumata et al., 2022), than in the AO– and CAI+ cases.

The relatively large sea ice outflow through the Fram Strait and S-FJL in winter–spring 2020 subsequently affected the

506 SIA and SIT in the BGS in the spring and early summer of 2020. In addition, the regional low air temperature anomalies during

507 February–April in the BGS favored the survival of sea ice there. Relatively large upward anomalies in atmospheric surface

508 heat fluxes dominated by turbulent heat flux in winter 2020, continuous upward anomalies in net longwave radiation in winter

509 and early spring 2020, and upward anomalies in net shortwave radiation in later spring 2020 can also reduce ice melting in the

510 BGS. In consequence, the monthly SIA in the BGS in April–June 2020 amounted to the first, second and fourth largest in

511 2010–2020, and the relatively large SIT over the BGS was observed since March 2020, especially in May–June. Sea ice

512 anomalies in the BGS subsequently influenced the oceanic conditions in the spring and early summer of 2020. In this region,

513 the SIA in April was significantly negatively correlated with the synchronous SST, as well as that with a lag of 1–3 months.

514 And the SST in April–June 2020 was the lowest in 2011–2020. The sea ice anomalies in the Barents Sea have a longer memory

515 for the impact on the SST than those in the Greenland Sea. Overall, the winter–spring Arctic sea ice outflow could be

516 considered a predictor that partially explain the changes in the conditions of sea ice and other marine environments in the BGS

517 in the subsequent months, at least until early summer.

518   The comparison with the years under similar (large) and contrary (small) scenarios of Arctic sea ice outflow confirmed

519 that the relationships between sea ice outflow anomalies and the oceanic conditions in the BGS identified in winter–spring

520 2020 is robust. In addition to the winter and spring seasons, the positive summer AO also enhances the summer Arctic sea ice

521 outflow to some extent, but demonstrates different regulatory mechanisms for the SIA in the BGS as there are obvious seasonal

522 variations in the atmospheric-ocean heat exchanges.

523   In this study, we mainly focused on the impact of atmospheric anomalies on the local sea ice mass balance in the BGS,

524 using only SST assimilated from observations and satellites to characterize the oceanic condition in the BGS, which is still

525 insufficient to gain insights into the dynamical and thermodynamic coupling mechanisms between sea ice and ocean. Therefore,

526 further collection of mooring and reanalysis records of ocean currents, ocean temperature and salinity, as well as in situ

527 observations of SST in the BGS, is recommended to characterize the influence mechanism of the increased Arctic sea ice

528 outflow on the seasonal evolutions of water transport, ocean stratification and ocean heat fluxes in the study region, which

529 could help to understand the interactions of the atmosphere-ice-ocean system in the BGS.

530 **Data Availability**

531 Sea ice motion data from the NSIDC is available at https://nsidc.org/data/NSIDC-0116/versions/4 (last access on 31 Dec

532 2021). NSIDC sea ice concentration data is obtained from https://nsidc.org/data/G02202/versions/4 (last access on 31 Dec

533 2021). The MOSAiC buoys data is available at https://data.meereisportal.de/data/buoys/. The IABP buoys data is

Author Contributions

FZ carried out the analysis, processed the data, and prepared the manuscript. RL provided the concept, discussed the results, and revised the manuscript during the writing process. All authors commented on the manuscript and finalized this paper.

Competing Interests

The authors declare that the research was conducted in the absence of any commercial or financial relationships that could be construed as a potential conflict of interest.

Financial support

This work was financially supported by the National Natural Science Foundation of China (grant nos. 41976219 and 42106231), the National Key Research and Development Program (grant nos. 2021YFC2803304 and 2018YFA0605903), and the Program of Shanghai Academic/Technology Research Leader (22XD1403600).

Reference

Banzon, V., Smith., T. M., Steele, M., Huang, B., and Zhang, H.-M.: Improved estimation of proxy sea surface temperature in the Arctic, J. Atmos. Oceanic Technol., 37, 341–349, https://doi.org/10.1175/JTECH-D-19-0177.1, 2020.

Bi, H., Sun, K., Zhou, X., Huang, H., and Xu, X.: Arctic Sea ice area export through the Fram Strait estimated from satellite-based data: 1988–2012, IEEE. J. Stars, 9(7), 3144–3157, https://doi.org/10.1109/jstars.2016.2584539, 2016.

Cai, L., Alexeev, V.A., and Walsh, J.E.: Arctic sea ice growth in response to synoptic- and large-scale atmospheric forcing from CMIP5 models, J. Clim., 33(14), 6083–6099. https://doi.org/10.1175/jcli-d-19-0326.1, 2020.

Cavalieri, D.J., Gloersen, P., and Campbell, W.J.: Determination of sea ice parameters with the Nimbus 7 SMMR, J. Geophys.

560   Res. Atmospheres., 89(D4), 5355–5369, https://doi.org/10.1016/0198-0254(84)93205-9, 1984.

561   Comiso, J.C.: Characteristics of Arctic winter sea ice from satellite multispectral microwave observations, J. Geophys. Res.
562   Oceans., 91(C1), 975–994, https://doi.org/10.1029/jc091ic01p00975, 1986.

563   de Steur, L., Hansen, E., Mauritzen, C., Beszczynska-Moeller, A., and Fahrbach, E.: Impact of recirculation on the East
564   Greenland Current in Fram Strait: Results from moored current meter measurements between 1997 and 2009, Deep-Sea
565   Research Part I-Oceanographic Research Papers, 92, 26–40, https://doi.org/10.1016/j.dsr.2014.05.018, 2014.

566   Dethloff, K., Maslowski, W., Hendricks, S., Lee, Y.J., Goessling, H.F., Krumpen, T., Haas, C., Handorf, D., Ricker, R., and
567   Bessonov, V.: Arctic sea ice anomalies during the MOSAiC winter 2019/20, The Cryosphere, 16(3), 981–1005,
568   https://doi.org/10.5194/tc-16-981-2022, 2022.

569   Dickson, R.R., Meincke, J., Malmberg, S.A.andLee, A.J.: The "Great Salinity Anomaly" in the Northern North-Atlantic 1968-
570   1982, Prog. Oceanogr., 20(2): 103–151, https://doi.org/10.1016/0079-6611(88)90049-3, 1988.

571   Dorr, J., Arthun, M., Eldevik, T., and Madonna, E.: Mechanisms of regional winter sea-ice variability in a warming Arctic, J.
572   Clim., 34(21), 8635–8653, https://doi.org/10.1175/jcli-d-21-0149.1, 2021.

573   Frey, K.E., Moore, G.W.K., Cooper, L.W., and Grebmeier, J.M.: Divergent patterns of recent sea ice cover across the Bering,
574   Chukchi, and Beaufort seas of the Pacific Arctic Region, Prog. Oceanogr., 136, 32–49,
575   https://doi.org/10.1016/j.pocean.2015.05.009, 2015.

576   Graham, R.M., Hudson, S.R., and Maturilli, M.: Improved performance of ERA5 in Arctic gateway relative to four global
577   atmospheric reanalyses, Geophys. Res. Lett., 46(11), 6138–6147, https://doi.org/10.1029/2019gl082781, 2019.

578   Hastenrath, S., & Greischar, L.: The North Atlantic oscillation in the NCEP-NCAR reanalysis, J. Clim., 14(11): 2404–2413,
579   https://doi.org/10.1175/1520-0442(2001)014<2404:TNAOIT>2.0.CO;2.

580   Hersbach, H., Bell, B., Berrisford, P., Hirahara, S., Horanyi, A., Munoz-Sabater, J., Nicolas, J., Peubey, C., Radu, R., Schepers,
581   D., Simmons, A., Soci, C., Abdalla, S., Abellan, X., Balsamo, G., Bechtold, P., Biavati, G., Bidlot, J., Bonavita, M., De
582   Chiara, G., Dahlgren, P., Dee, D., Diamantakis, M., Dragani, R., Flemming, J., Forbes, R., Fuentes, M., Geer, A.,
583   Haimberger, L., Healy, S., Hogan, R.J., Holm, E., Janiskova, M., Keeley, S., Laloyaux, P., Lopez, P., Lupu, C., Radnoti,
584   G., de Rosnay, P., Rozum, I., Vamborg, F., Villaume, S., and Thepaut, J.N.: The ERA5 global reanalysis, Q. J. Roy. Meteor.
585   Soc., 146(730), 1999–2049, https://doi.org/10.1002/qj.3803, 2020.

586   Huang, B., Liu, C., Banzon, V., Freeman, E., Graham, G., Hankins, B., Smith, T., and Zhang, H.M.: Improvements of the Daily
587   Optimum Interpolation Sea Surface Temperature (DOISST) Version 2.1, J. Clim., 34, 2923–2939,
588   https://doi.org/10.1175/JCLI-D-20-0166.1, 2021.

589   Hurrell, J.W.: Climate and climate change| Climate variability: North Atlantic and Arctic oscillation, in: Encyclopedia of
590   Atmospheric Sciences (Second Edition), edited by: North, G.R., Pyle, J. and Zhang, F., Oxford: Academic Press, 47–60,
591   https://doi.org/10.1016/B978-0-12-382225-3.00109-2, 2015.

592   Krumpen, T., Birrien, F., Kauker, F., Rackow, T., von Albedyll, L., Angelopoulos, M., Belter, H. J., Bessonov, V., Damm, E.,
593   Dethloff, K., Haapala, J., Haas, C., Harris, C., Hendricks, S., Hoelemann, J., Hoppmann, M., Kaleschke, L., Karcher,
594   M., Kolabutin, N., Lei, R., Lenz, J., Morgenstern, A., Nicolaus, M., Nixdorf, U., Petrovsky, T., Rabe, B., Rabenstein, L.,
595   Rex, M., Ricker, R., Rohde, J., Shimanchuk, E., Singha, S., Smolyanitsky, V., Sokolov, V., Stanton, T., Timofeeva, A.,

Tsamados, M., and Watkins, D.: The MOSAiC ice floe: Sediment-laden survivor from the Siberian shelf, The Cryosphere, 14(7), 2173–2187, http://dx.doi.org/10.5194/tc-14-2173-2020, 2020.

Krumpen, T., von Albedyll, L., Goessling, H.F., Hendricks, S., Juhls, B., Spreen, G., Willmes, S., Belter, H.J., Dethloff, K., Haas, C., Kaleschke, L., Katlein, C., Tian-Kunze, X., Ricker, R., Rostosky, P., Rueckert, J., Singha, S., and Sokolova, J.: MOSAiC drift expedition from October 2019 to July 2020: sea ice conditions from space and comparison with previous years, The Cryosphere, 15(8), 3897–3920, https://doi.org/10.5194/tc-15-3897-2021, 2021.

Kwok, R.: Outflow of Arctic ocean sea ice into the Greenland and Barents Seas: 1979–2007, J. Clim., 22(9), 2438–2457, https://doi.org/10.1175/2008jcli2819.1, 2009.

Kwok, R., Cunningham, G., Wensnahan, M., Rigor, I., Zwally, H., and Yi, D.: Thinning and volume loss of the Arctic Ocean sea ice cover: 2003–2008, J. Geophys. Res. Oceans., 114(C7), https://doi.org/10.1029/2009jc005312, 2009.

Kwok, R., Spreen, G. and Pang, S.: Arctic sea ice circulation and drift speed: decadal trends and ocean currents. J. Geophys. Res. Oceans., 118(5), 2408–2425, https://doi.org/10.1002/jgrc.20191, 2013.

Lei, R., Gui, D., Hutchings, J.K., Wang, J., and Pang, X.: Backward and forward drift trajectories of sea ice in the northwestern Arctic Ocean in response to changing atmospheric circulation, Int. J. Climatol., 39(11), 4372–4391, https://doi.org/10.1002/joc.6080, 2019.

Lei, R., Heil, P., Wang, J., Zhang, Z., Li, Q., and Li, N.: Characterization of sea-ice kinematic in the Arctic outflow region using buoy data, Polar. Res., 35(1), https://doi.org/10.3402/polar.v35.22658, 2016.

Lind, S., Ingvaldsen, R.B., and Furevik, T.: Arctic warming hotspot in the northern Barents Sea linked to declining sea-ice import. Nat. Clim. Change., 8(7), 634–639, https://doi.org/10.1038/s41558-018-0205-y, 2018.

Mayot, N., Matrai, P.A., Arjona, A., Belanger, S., Marchese, C., Jaegler, T., Ardyna, M., and Steele, M.: Springtime export of Arctic sea ice influences phytoplankton production in the Greenland Sea, J. Geophys. Res. Oceans., 125(3), https://doi.org/10.1029/2019jc015799, 2020.

Meier, W.N., Fetterer, F., Windnagel, A.K., and Stewart, J.S.: NOAA/NSIDC Climate Data Record of Passive Microwave Sea Ice Concentration, Version 4, Boulder, Colorado USA. NSIDC: National Snow and Ice Data Center, https://doi.org/10.7265/efmz-2t65, 2021.

Minnett, P.J., and Key, E.L.: Meteorology and atmosphere–surface coupling in and around polynyas, Elsevier Oceanography Series, 74, 127–161, https://doi.org/10.1016/S0422-9894(06)74004-1, 2007.

Mori, M., Watanabe, M., Shiogama, H., Inoue, J., and Kimoto, M.: Robust Arctic sea-ice influence on the frequent Eurasian cold winters in past decades, Nat. Geosci., 7(12), 869–873, https://doi.org/10.1038/ngeo2277, 2014.

Mørk, T., Bohlin, J., Fuglei, E., Asbakk, K., and Tryland, M.: Rabies in the arctic fox population, Svalbard, Norway, J. Wildlife. Dis., 47(4), 945–957, https://doi.org/10.7589/0090-3558-47.4.945, 2011.

Nicolaus, M., Riemann-Campe, K., Hutchings, J.K., Granskog, M.A., Krishfield, R., Lei, R., Li, T., and Rabe, B.: Drift trajectories of the main sites of the Distributed Network and the Central Observatories of MOSAiC 2019/2020, Epic, 2021.

Onarheim, I.H., Eldevik, T., Smedsrud, L.H., and Stroeve, J.C.: Seasonal and regional manifestation of Arctic sea ice loss, J.

631   Clim., 31(12), 4917–4932, https://doi.org/10.1175/jcli-d-17-0427.1, 2018.

632   Pabi, S., van Dijken, G.L.and Arrigo, K.R.: Primary production in the Arctic Ocean, 1998-2006, J. Geophys. Res. Oceans.,

633   113(C8), https://doi.org/10.1029/2007JC004578, 2008.

634   Parkinson, C.L., and DiGirolamo, N.E.: Sea ice extents continue to set new records: Arctic, Antarctic, and global results,

635   Remote. Sens. Environ., 267: 112753, https://doi.org/10.1016/j.rse.2021.112753, 2021.

636   Parkinson, C.L., and Washington, W.M.: A large-scale numerical model of sea ice, J. Geophys. Res. Oceans., 84(C1), 311–337,

637   https://doi.org/10.1029/JC084iC01p00311, 1979.

638   Peeken, I., Primpke, S., Beyer, B., Gutermann, J., Katlein, C., Krumpen, T., Bergmann, M., Hehemann, L., and Gerdts, G.:

639   Arctic sea ice is an important temporal sink and means of transport for microplastic, Nat. Commun., 9,

640   https://doi.org/10.1038/s41467-018-03825-5, 2018.

641   Peng, G., Meier, W.N., Scott, D.J., and Savoie, M.H.: A long-term and reproducible passive microwave sea ice concentration

642   data record for climate studies and monitoring, Earth. Syst. Sci. Data., 5(2), 311–318, https://doi.org/10.5194/essd-5-311-

643   2013, 2013.

644   Polyakov, I.V., Ingvaldsen, R.B., Pnyushkov, A.V., Bhatt, U.S., Francis, J.A., Janout, M., Kwok, R.and Skagseth, Ø.:

645   Fluctuating   Atlantic   inflows   modulate   Arctic   atlantification,   Science,   381(6661):   972-979,

646   https://doi.org/10.1126/science.adh5158, 2023.

647   Previdi, M., Smith, K.L., and Polvani, L.M.: Arctic amplification of climate change: a review of underlying mechanisms,

648   Environ. Res. Lett., 16(9), https://doi.org/10.1088/1748-9326/ac1c29, 2021.

649   Rahmstorf, S., Box, J.E., Feulner, G., Mann, M.E., Robinson, A., Rutherford, S.and Schaffernicht, E.J.: Exceptional twentieth-

650   century   slowdown   in   Atlantic   Ocean   overturning   circulation,   Nat.   Clim.   Change.,   5(5):   475–480,

651   https://doi.org/10.1038/NCLIMATE2554, 2015.

652   Reynolds, R.W., Smith, T.M., Liu, C., Chelton, D.B., Casey, K.S., and Schlax, M.G.: Daily high-resolution-blended analyses

653   for sea surface temperature, J. Clim., 20(22), 5473–5496, https://doi.org/10.1175/2007jcli1824.1, 2007.

654   Ricker, R., Hendricks, S., Kaleschke, L., Tian-Kunze, X., King, J., and Haas, C.: A weekly Arctic sea-ice thickness data record

655   from merged CryoSat-2 and SMOS satellite data, The Cryosphere, 11(4), 1607–1623, https://doi.org/10.5194/tc-11-1607-

656   2017, 2017.

657   Ricker, R., Kauker, F., Schweiger, A., Hendricks, S., Zhang, J., and Paul, S.: Evidence for an increasing role of ocean heat in

658   Arctic winter sea ice growth, J. Clim., 34(13), 5215–5227, https://doi.org/10.1175/jcli-d-20-0848.1, 2021.

659   Rigor, I.G., Wallace, J.M., and Colony, R.L.: Response of sea ice to the Arctic Oscillation, J. Clim., 15(18), 2648–2663,

660   https://doi.org/10.1029/1999gl002389, 2002.

661   Sathyendranath, S., Jackson, T., Brockmann, C., Brotas, V., Calton, B., Chuprin, A., Clements, O., Cipollini, P., Danne, O.,

662   Dingle, J., Donlon, C., Grant, M., Groom, S., Krasemann, H., Lavender, S., Mazeran, C., Melin, F., Muller, D., Steinmetz,

663   F., Valente, A., Zuhlke, M., Feldman, G., Franz, B., Frouin, R., Werdell, J., and Platt, T.: ESA Ocean Colour Climate

Change Initiative (Ocean_Colour_cci): Version 5.0 Data, Centre for Environmental Data Analysis, https://doi.org/10.5285/1dbe7a109c0244aaad713e078fd3059a, 2021.

Schlichtholz, P.: Subsurface ocean flywheel of coupled climate variability in the Barents Sea hotspot of global warming, Sci. Rep., 9(1), 1–16, https://doi.org/10.1038/s41598-019-49965-6, 2019.

Schweiger, A., Lindsay, R., Zhang, J.L., Steele, M., Stern, H., and Kwok, R.: Uncertainty in modeled Arctic sea ice volume, J. Geophys. Res. Oceans., 116(C8), https://doi.org/10.1029/2011jc007084, 2011.

Shu, Q., Wang, Q., Song, Z., and Qiao, F.: The poleward enhanced Arctic Ocean cooling machine in a warming climate, Nat. Commun., 12(1), https://doi.org/10.1038/s41467-021-23321-7, 2021.

Siswanto, E.: Temporal variability of satellite-retrieved chlorophyll-a data in Arctic and subarctic ocean regions within the past two decades, Int. J. Remote. Sens., 41(19), 7427–7445, https://doi.org/10.1080/01431161.2020.1759842, 2020.

Smedsrud, L.H., Esau, I., Ingvaldsen, R.B., Eldevik, T., Haugan, P.M., Li, C., Lien, V.S., Olsen, A., Omar, A.M., and Otterå, O.H.: The role of the Barents Sea in the Arctic climate system, Rev. Geophy., 51(3), 415–449, https://doi.org/10.1017/cbo9780511535888.008, 2013.

Smedsrud, L.H., Halvorsen, M.H., Stroeve, J.C., Zhang, R., and Kloster, K.: Fram Strait sea ice export variability and September Arctic sea ice extent over the last 80 years, The Cryosphere, 11(1): 65–79, https://doi.org/10.5194/tc-11-65-2017, 2017.

Spreen, G., Kern, S., Stammer, D., and Hansen, E.: Fram Strait sea ice volume export estimated between 2003 and 2008 from satellite data, Geophys. Res. Lett., 36(19), https://doi.org/10.1029/2009GL039591, 2009.

Stroeve, J., Barrett, A., Serreze, M., and Schweiger, A.: Using records from submarine, aircraft and satellites to evaluate climate model simulations of Arctic sea ice thickness, The Cryosphere, 8(5), 1839–1854, https://doi.org/10.5194/tc-8-1839-2014, 2014.

Sumata, H., de Steur, L., Gerland, S., Divine, D. V., and Pavlova, O.: Unprecedented decline of Arctic sea ice outflow in 2018. Nat. Commun., 13(1), 1747, https://doi.org/10.1038/s41467-022-29470-7, 2022.

Thompson, D.W.J., and Wallace, J.M. : The Arctic Oscillation signature in the wintertime geopotential height and temperature fields, Geophys. Res. Lett., 25(9), 1297–1300, https://doi.org/10.1029/98gl00950, 1998.

Tschudi, M.A,, Meier, W.N., Stewart, J.S., Fowler, C., and Maslanik, J.: Polar Pathfinder Daily 25 km EASE-Grid Sea Ice Motion Vectors, Version 4, Boulder, Colorado USA, NASA National Snow and Ice Data Center Distributed Active Archive Center, https://doi.org/10.5067/INAWUWO7QH7B, 2019.

Tschudi, M.A., Meier, W.N., and Stewart, J.S.: An enhancement to sea ice motion and age products at the National Snow and Ice Data Center (NSIDC), The Cryosphere, 14(5), 1519–1536, https://doi.org/10.5194/tc-14-1519-2020, 2020.

Vihma, T., Tisler, P., and Uotila, P.: Atmospheric forcing on the drift of Arctic sea ice in 1989–2009, Geophys. Res. Lett., 39(2), https://doi.org/10.1029/2011gl050118, 2012.

Wang, X., Key, J., Kwok, R., and Zhang, J.: Comparison of Arctic sea ice thickness from satellites, aircraft, and PIOMAS data, Remote Sens., 8(9), https://doi.org/10.3390/rs8090713, 2016.

698 Wang, Y., Bi, H., Huang, H., Liu, Y., Liu, Y., Liang, X., Fu, M., and Zhang, Z.: Satellite-observed trends in the Arctic sea ice
699   concentration for the period 1979–2016, J. Oceanol. Limnol., 37(1), 18–37, https://doi.org/10.1007/s00343-019-7284-0,
700   2019.

701 Wassmann, P., Slagstad, D., and Ellingsen, I.: Primary production and climatic variability in the European sector of the Arctic
702   Ocean prior to 2007: preliminary results, Polar. Biol., 33(12), 1641–1650, https://doi.org/10.1007/s00300-010-0839-3,
703   2010.

704 Zhang, F., Pang, X., Lei, R., Zhai, M., Zhao, X., and Cai, Q.: Arctic sea ice motion change and response to atmospheric forcing
705   between 1979 and 2019, Int. J. Climatol., 42(3), 1854–1876, https://doi.org/10.1002/joc.7340, 2022.

706 Zhang, J. and Rothrock, D.A.: Modeling global sea ice with a thickness and enthalpy distribution model in generalized
707   curvilinear coordinates, Mon. Weather. Rev., 131(5), 845–861, https://doi.org/10.1175/1520-
708   0493(2003)131<0845:mgsiwa>2.0.co;2, 2003.

709 Zhang, S., Gan, T. and Bush, A.B.G.: Variability of Arctic Sea Ice Based on Quantile Regression and the Teleconnection with
710   Large-Scale Climate Patterns, J. Clim., 33(10), 4009-4025, https://doi.org/10.1175/JCLI-D-19-0375.1, 2020.

711 **Appendix A: Extra figures and tables**
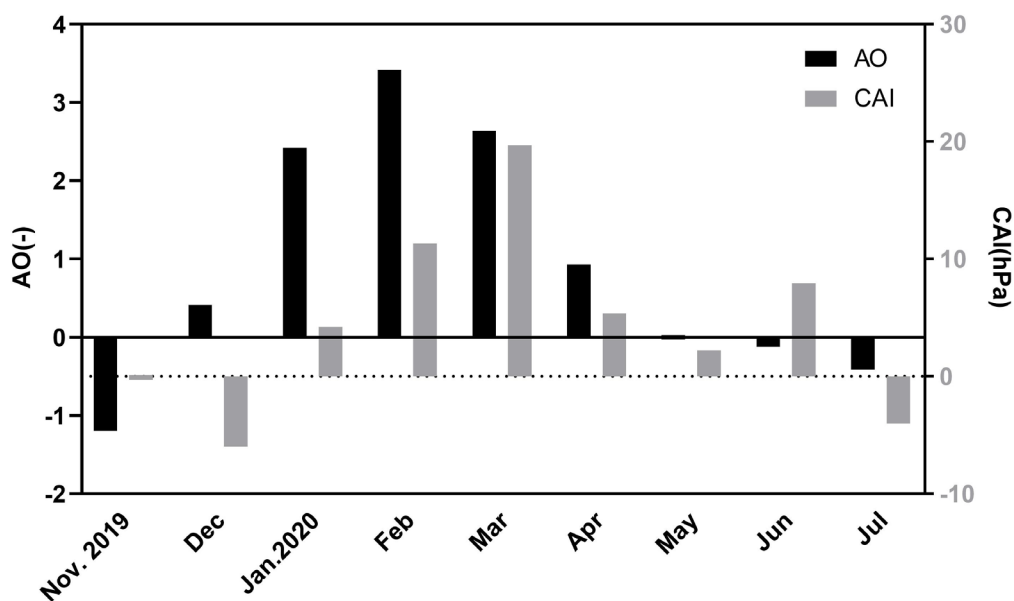
712

713 **Figure A1.** Time series of the monthly AO index (black bar) and CAI (gray bar) from November 2019 to July 2020.
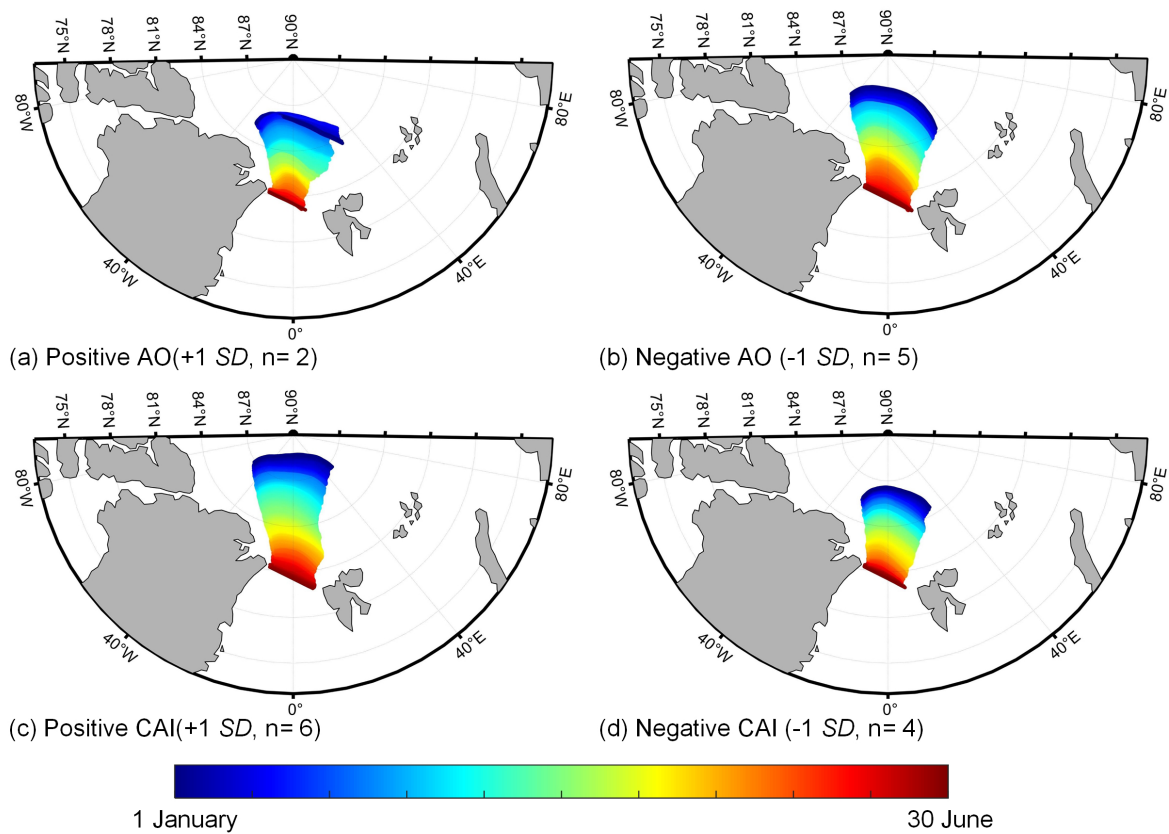
714

715   **Figure A2.** Sea ice backward trajectories from the Fram Strait under the extremely positive and negative phases of the AO and CAI in 1988–

716   2020. An extremely positive (negative) phase is defined as the value of the index higher (lower) than climatological values by 1 *SD*. Numbers

717   represent the number of years with extremely positive or negative phase of the atmospheric circulation indices. Color coding of the sea ice

718   backward trajectories denotes the time from 1 January to 30 June.

719   **Table A1.** Correlation coefficient (*R*) between monthly sea ice motion speed and wind speed in the Atlantic sector of TPD for 1979–2020

Month	January	February	March	April	May	June
R	*0.411*	0.355	n.s.	*0.478*	n.s.	**0.493**

720   Note: Significance levels are *P* < 0.001 (bold), *P* < 0.01 (italic) and *P* < 0.05 (plain); n.s. denotes insignificant at the 0.05 level.

721   **Table A2**. Consistency of reconstructed sea ice backward trajectories with buoy trajectories

Different condition	Year	Average Euclidean distance (km)	Average cosine similarity (-)
Study year	2020	63.3±25.5	0.85±0.25
AO+	2015	1177.0±909.6	0.93±0.12
CAI+	2019	897.4±621.9	0.91±0.16
AO–	2012	1369.0±356.2	0.99±0.02
CAI–	2010	1493.5±1082.4	0.99±0.04

722 **Table A3.** Synchronous correlation coefficient (R) between monthly sea ice area (SIA) and sea surface temperature (SST) in April, May, or
723 June for 1982–2020.

	Month	All	North(76°–80°N)	South(72°–76°N)
Barents Sea	April	**−0.924**	**−0.780**	**−0.921**
	May	**−0.835**	**−0.715**	**−0.805**
	June	**−0.754**	**−0.681**	**−0.711**
Greenland Sea	April	**−0.641**	n.s.	−0.366
	May	**−0.654**	n.s.	*−0.379*
	June	**−0.659**	n.s.	n.s.

724 Note: Significance levels are $P < 0.001$ (bold), $P < 0.01$ (italic) and $P < 0.05$ (plain); n.s. denotes insignificant at the 0.05 level.

725 **Table A4**. Lagging correlation coefficient (R) between monthly sea ice area (SIA) in April and sea surface temperature (SST) in May, June,
726 or July for 1982–2020.

	Month	All	North(76°–80°N)	South(72°–76°N)
Barents Sea	May	**−0.863**	**−0.656**	**−0.878**
	June	**−0.757**	**−0.643**	**−0.741**
	July	*−0.478*	**−0.548**	−0.372
Greenland Sea	May	**−0.560**	n.s.	n.s.
	June	*−0.434*	n.s.	n.s.
	July	n.s.	n.s.	n.s.

727 Note: Significance levels are $P < 0.001$ (bold), $P < 0.01$ (italic) and $P < 0.05$ (plain); n.s. denotes insignificant at the 0.05 level.

728 **Table A5.** Correlation coefficient (R) between the latitude or longitude of endpoint of sea ice backward trajectory from the Fram Strait and
729 atmospheric circulation indices in 1988–2020.

Investigation period	January–April	January–May	January–June

Lat *vs.* AO	n.s.	0.354	0.347
Lon *vs.* AO	n.s.	−0.419	*−0.514*
Lat *vs.* CAI	n.s.	**0.625**	**0.590**
Lon *vs.* CAI	n.s.	*−0.508*	**−0.599**

730   Note: Significance levels are $P < 0.001$ (bold), $P < 0.01$ (italic) and $P < 0.05$ (plain); n.s. denotes insignificant at the 0.05 level.